Maastricht University

# The potential of MR-Encephalography for BCI/Neurofeedback applications with high temporal resolution

Citation for published version (APA):

**Document status and date:**
Published: 01/07/2019

**DOI:**

**Document Version:**
Publisher's PDF, also known as Version of record

**Document license:**
Taverne

**Please check the document version of this publication:**

• A submitted manuscript is the version of the article upon submission and before peer-review. There can be important differences between the submitted version and the official published version of record. People interested in the research are advised to contact the author for the final version of the publication, or visit the DOI to the publisher's website.
• The final author version and the galley proof are versions of the publication after peer review.
• The final published version features the final layout of the paper including the volume, issue and page numbers.

**Link to publication**

Download date: 30 Apr. 2024

# The potential of MR-Encephalography for BCI/Neurofeedback applications with high temporal resolution

Michael Lührs [a,b,c,*], Bruno Riemenschneider [f], Judith Eck [a,b,c], Amaia Benitez Andonegui [a,b], Benedikt A. Poser [a,b], Armin Heinecke [a,b,c], Florian Krause [a,b,d], Fabrizio Esposito [a,b,e], Bettina Sorger [a,b], Jürgen Hennig [f], Rainer Goebel [a,b,c,g]

[a] Faculty of Psychology and Neuroscience, Department of Cognitive Neuroscience, Maastricht University, the Netherlands
[b] Maastricht Brain Imaging Center, Maastricht, the Netherlands
[c] Brain Innovation B.V., Research Department, Maastricht, the Netherlands
[d] Department of Cognitive Neuroscience, Donders Institute for Brain, Cognition and Behaviour, Radboud University Medical Center, Nijmegen, the Netherlands
[e] Department of Medicine, Surgery and Dentistry, Scuola Medica Salernitana, University of Salerno, Baronissi (SA), Italy
[f] Dept. of Radiology, Medical Physics, Medical Center – University of Freiburg, Faculty of Medicine, University of Freiburg, Germany
[g] Netherlands Institute for Neuroscience (NIN), Amsterdam, the Netherlands

## ARTICLE INFO

## ABSTRACT

Real-time functional magnetic resonance imaging (rt-fMRI) enables the update of various brain-activity measures during an ongoing experiment as soon as a new brain volume is acquired. However, the recorded Blood-oxygen-level dependent (BOLD) signal also contains physiological artifacts such as breathing and heartbeat, which potentially cause misleading false positive effects especially problematic in brain-computer interface (BCI) and neurofeedback (NF) setups. The low temporal resolution of echo planar imaging (EPI) sequences (which is in the range of seconds) prevents a proper separation of these artifacts from the BOLD signal. MR-Encephalography (MREG) has been shown to provide the high temporal resolution required to unalias and correct for physiological fluctuations and leads to increased specificity and sensitivity for mapping task-based activation and functional connectivity as well as for detecting dynamic changes in connectivity over time. By comparing a simultaneous multislice echo planar imaging (SMS-EPI) sequence and an MREG sequence using the same nominal spatial resolution in an offline analysis for three different experimental fMRI paradigms (perception of house and face stimuli, motor imagery, Stroop task), the potential of this novel technique for future BCI and NF applications was investigated. First, adapted general linear model pre-whitening which accounts for the high temporal resolution in MREG was implemented to calculate proper statistical results and be able to compare these with the SMS-EPI sequence. Furthermore, the respiration- and cardiac pulsation-related signals were successfully separated from the MREG signal using independent component analysis which were then included as regressors for a GLM analysis. Only the MREG sequence allowed to clearly separate cardiac pulsation and respiration components from the signal time course. It could be shown that these components highly correlate with the recorded respiration and cardiac pulsation signals using a respiratory belt and fingertip pulse plethysmograph. Temporal signal-to-noise ratios of SMS-EPI and MREG were comparable. Functional connectivity analysis using partial correlation showed a reduced standard error in MREG compared to SMS-EPI. Also, direct time course comparisons by downsampling the MREG signal to the SMS-EPI temporal resolution showed lower variance in MREG. In general, we show that the higher temporal resolution is beneficial for fMRI time course modeling and this aspect can be exploited in offline application but also, is especially attractive, for real-time BCI and NF applications.

## 1. Introduction

Recent technological advances in computational power and the advent of more sophisticated image reconstruction techniques over the last years made it possible to use higher spatial and temporal resolutions in functional brain imaging with MRI (Feinberg et al., 2010; Poser and Setsompop, 2018; Rabrait et al., 2008). However, these new possibilities also require more advanced preprocessing and statistical computations,

such as handling auto-correlations across many volumes, to fulfill the requirements for the commonly used parametric statistical analyses (Fadili et al., 2003). Specific advancements in the field of functional magnetic resonance imaging (fMRI) provided new acquisition methods such as simultaneous multi-slice (SMS, also known as multi-band, MB) (Feinberg et al., 2010; Feinberg and Setsompop, 2013), blipped controlled aliasing (CAIPI) EPI blipped-CAIPI-EPI) (Moeller et al., 2010; Setsompop et al., 2012), echo volumar imaging EVI (Rabrait et al., 2008), multi-slab EVI (Posse et al., 2012) or simultaneous multi-slice inverse imaging (SMS-InI) (Hsu et al., 2017), allowing to acquire fMRI data using repetition times (TR) in the range of hundreds of milliseconds and are also suitable for real-time applications. The method used in this article to perform fMRI is called MR-Encephalography (MREG) (Hennig et al., 2007). It is of particular interest for real-time applications because it allows to use a very high temporal resolution of 100 ms (and possible even up to 25 ms). To be more precise, the higher temporal resolution is a crucial factor to increase sensitivity, specificity and signal-to-noise ratios (SNR) with respect to confounding signals, as physiological noise can be separated from the signal of interest (Assländer et al., 2013; Feinberg and Setsompop, 2013; Feinberg and Yacoub, 2012; Lee et al., 2013; Lewis et al., 2016; Lin et al., 2012; Posse et al., 2013; Zahneisen et al., 2011). This is possible since the high temporal resolution allows to record these confounding signals and with this gives the possibilty to remove these components from the signal of interest. Additionally, since most sequences that allow sub-second TRs are also suitable for real-time fMRI data analysis (possible image reconstruction within a TR), MREG should be regarded as a potential candidate in real-time setups. MREG combines the sampling efficiency of non-Cartesian trajectories with under-sampled variable density read-outs to achieve ultra-fast fMRI acquisition (Assländer et al., 2013; Hennig et al., 2007; Zahneisen et al., 2011, 2012). In conjunction with recent parallel receiver arrays this permits repetition times below 100 ms for whole-brain fMRI. This approach trades off some spatial resolution and introduces susceptibility artifacts in the presence of strong off-resonance gradients to achieve the ultra-fast read-out (Assländer et al., 2013). The clear downside of highly-undersampled non-Cartesian acquisition is their significantly higher computational burden compared echo-planar acquisitions. As a consequence, for MREG there is currently no solution to fully reconstruct each frame in real-time (i.e., in less than 100 ms). Even strong cluster computers are not able to fulfill the criteria of reconstructing data within a single TR. To overcome this computational issue, a novel real-time MREG (rtMREG) method was recently introduced, which creates a time course of interest from preselected brain areas using one individual reconstruction vector per ROI (LI, 2014; Riemenschneider et al., 2019; Riemenschneider et al., 2015). The real-time access of predefined areas is made possible through minimal reconstructions that only extract mean values from ROIs by an incomplete basis change of the reconstruction matrix. The minimal reconstructions, which are performed by one simple dot product per ROI per frame, require pre-calculations that are independent of the main experiment's signal data and can be performed beforehand.

In the current study, we performed an offline analysis to demonstrate the potential of MREG and specifically encourage the use for real-time applications such as brain-computer interfaces (BCI's) and, more specifically, neurofeedback (NF). To be able to identify specific differences between MREG and SMS-EPI-sequence parameters, we conducted three different experiments, each of them twice in a counter-balanced fashion across participants which were then analyzed offline: Once with a SMS-EPI sequence using a TR of 2000 ms and once using an MREG sequence with a temporal resolution of 100 ms. This allowed to directly investigate the individual differences in single subjects as well as group differences using the two sequences. In addition, we examined the overall differences of both sequences with respect to co-registration of anatomical and functional data as well as preprocessing and analysis methods. A first analysis focused on the statistical properties of SMS-EPI and MREG data using the standard general linear model (GLM), which is commonly used in fMRI data analyses (Monti, 2011). A second analysis focused on the

temporal signal to noise ratio (tSNR) of SMS-EPI and MREG data. Eventually, a third analysis explored the potentials of high temporal resolution acquisitions with respect to functional connectivity analysis. The functional connectivity analysis has become more popular in recent years in real-time fMRI applications (Bastos and Schoffelen, 2016; Karl J. Friston, 2011; Hutchison et al., 2013; Zilverstand et al., 2014). The connectivity between different brain regions can be used to strengthen functional connections to support rehabilitation processes (Canuet, 2015; Díez-Cirarda et al., 2017; Ochmann et al., 2017) or can give different insights than standard univariate analysis. Having a higher temporal resolution can be beneficial, e.g., for dynamic functional connectivity in event-based paradigms as shown by (Sahib et al., 2018) and gives more reliable connectivity results (Karahanoğlu & Van De Ville, 2017). We aimed to show the direct benefit of MREG for real-time applications along the preprocessing and analysis pipeline, since this method was not yet applied in a BCI environment. Even the possibility to provide NF in a common (e.g., thermometer (Krause et al., 2017); fashion, but use MREG with this very high temporal resolution will certainly have benefits for offline analysis as we will show in this article.

### 1.1. Proposed real-time study setup

Due to the computationally extensive image reconstruction time of MREG it is not possible to analyze a functional localizer within the current session. A dedicated functional localizer session is advised, unless only anatomical information will be used, to define a target region. When opting for a functional target region of interest (ROI) localizer session on a different day, as described below, the data needs to be analyzed offline before the actual real-time session. This way, potential signal shifts, which are characteristic for any k-space trajectory, are already accounted for in the extracted target regions. On both scanning days, anatomical reference datasets need to be acquired for the co-registration of the ROIs. On the second day, the previously localized ROIs can be aligned to the current position of the subject using a transformation matrix created by registering the anatomical datasets from day one and day two as shown in Fig. 1.

The matrix of the ROI-specific targeted partial reconstruction can be pre-computed right at the beginning of the actual real-time session and will then be applied for NF purposes during subsequent functional runs. The targeted Partial Reconstruction was applied using a partial SENSE method for the MREG acquisition. This generates minimal reconstructions of the sums over one or several freely selected ROI's (Riemenschneider et al., 2019). One reconstruction vector is computed per target, each obtained by a full iterative reconstruction prior to the experiment. Each reconstruction vector then allows to reconstruct the signal from its target region as a scalar product. More details about the partial SENSE method and the partial reconstruction can be found in the corresponding publication (Riemenschneider et al., 2019).

The reconstruction results can be exported in real-time using e.g., a direct TCP/IP stream, which avoids potential delays possible when using a usual file transfer. To be able to receive the data directly a re-routing (e.g., 'tunneling') from the image reconstruction computer through the MRI console computer needs to be integrated, which can be realized by port forwarding from the image reconstruction computer to the real-time processing computer via the MRI console.

## 2. Methods

In this section we will cover the methods used to point out the differences between SMS-EPI and MREG data with respect to future real-time processing and the differences introduced by the high sampling rate.

### 2.1. Participants

Twelve healthy volunteers (six females; all recruited at Maastricht University, Maastricht, the Netherlands) aged between 23 and 39 years
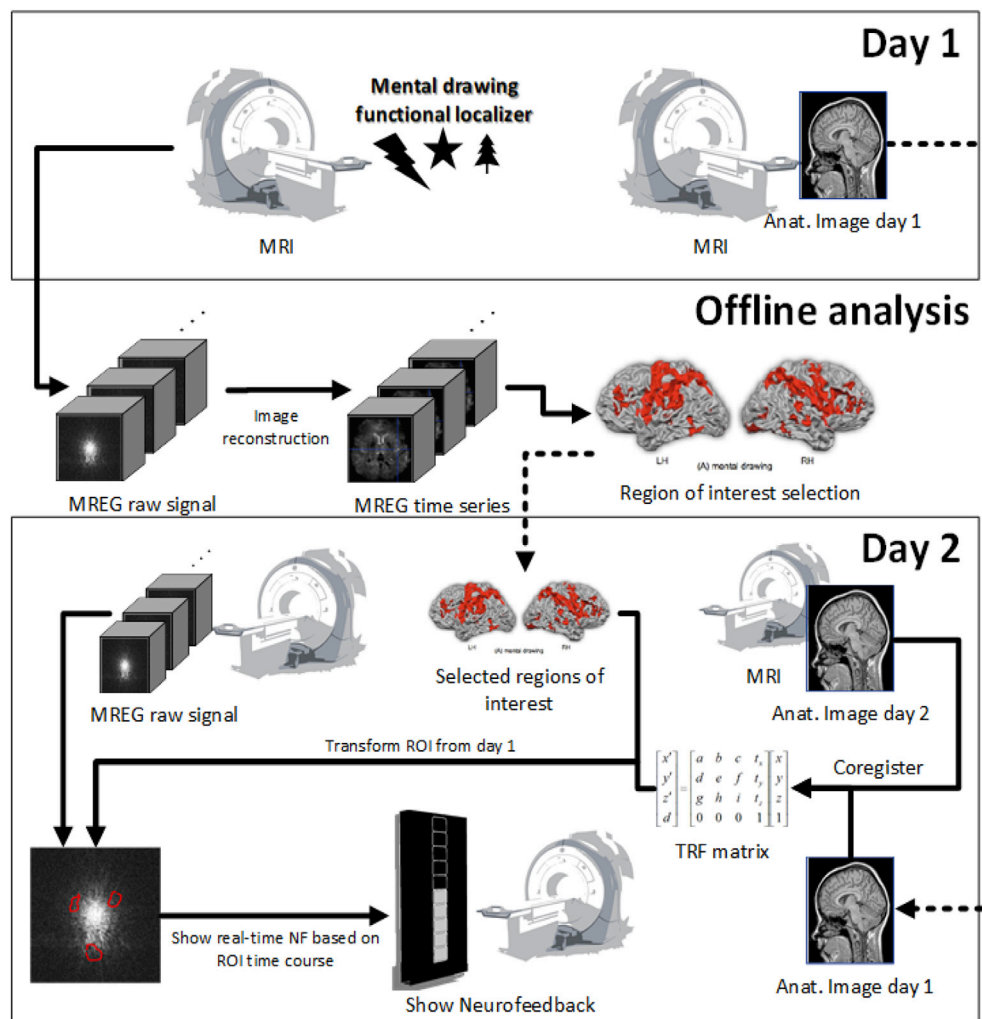
**Fig. 1.** Workflow of rtMREG experiments. During the first day a localizer and anatomical scan is performed. At day two another anatomy is scanned for corregistration and localizing the region defined on the first day.

(mean = 28; SD = 4.97) participated in the three experiments. All participants had normal or corrected-to-normal vision and had no history of neurological or psychological disorders. The volunteers were informed about the details of the study and the two different sequences. The study was approved by the local ethics committee, and participants gave their written informed consent before participating in the study.

### 2.2. Study design

All participants performed the same three tasks in pseudo-randomized order. The first task was a motor imagery paradigm consisting of eight task and nine rest blocks each lasting 24s. During the task blocks the participants were asked to draw a simple figure or object in their mind using the right hand (Lührs et al., 2017; Sorger et al., 2012). Objects were for example stars, trees or cars that were easy to imagine for each person individually. The second task was a passive viewing task where the participants had to focus on the center of the screen while pictures of faces or houses were shown (Kanwisher et al., 1997). Picture blocks had alternating faces and houses every 500 ms, with a total duration of 16s. The rest blocks in between the picture blocks lasted 16s as well. The third paradigm was a standard color-based Stroop task (Peterson et al., 1999). Participants had to press either the index finger for red colored text or the middle finger if the text color was green, while ignoring the semantic meaning of the text ("RED" or "GREEN") which was presented in the center of the screen. The slowest reaction time was set to

1.5s and randomized stimulus interval ranging from 500 ms to 16s.

Each run lasted 400 s for SMS-EPI and MREG. Each experiment was performed twice, once with SMS-EPI sequence and once with MREG. The whole experiment took approximately one hour for each participant including an additional anatomical scan.

### 2.3. MRI data acquisition

All data were acquired using a 3T MRI full body scanner (PRISMA fit, MR_VE11C, Siemens Healthcare, Erlangen, Germany) equipped with a 64-channel head coil. All sessions were scanned with the same scanning parameters for all participants. For the EPI data a simultaneous multislice sequence (Barth et al., 2016; Feinberg et al., 2010; Moeller et al., 2010; Setsompop et al., 2012) was used where the scanning parameters were as follows: 200 vol, TR/TE = 2000 ms/30 ms, flip angle 77°, matrix size = 64 × 64 using a 192 × 192 mm field of view (FOV), multiband factor 2, 50 × 3.0-mm slices without gap. The MREG acquisition covered the exact same FOV as the SMS-EPI, with an isotropic nominal resolution of 3 mm resulting in a matrix size of 64 × 64 × 50, TR = 100 ms, flip angle of 23°, for 4000 volumes. We used a single-shot spherical stack-of-spirals trajectory for the read-out, as described in (Assländer et al., 2013). The data was reconstructed offline after the recording. The reference scans were based on a gradient echo sequences (GRE) used for anatomical reference and calculation of the sensitivity maps for the MREG reconstruction had the following parameters:

TR/TE = 381 ms/2.46 ms, flip angle 25°, matrix = 128 × 128 using a 192 × 192 mm field of view (FOV), 100 × 0.5-mm slices without gap.

Physiological signals (pulse oximetry, and respiratory depth) were recorded using the MR system's built-in wireless fingertip pulse plethysmograph and respiratory belt at 50 Hz. For each participant, a MPRAGE T1-weighted anatomical data set encompassing the whole brain was acquired following the localizer experiment (scan parameters: TR = 2250 ms, TE = 2.21 ms, FA = 9°, FOV = 256 × 256mm2, matrix size = 256 × 256, number of slices = 192, slice thickness = 1 mm, total scan time = 8min and 26s).

SMS-EPI and MREG data preprocessing included motion correction and temporal filtering using BrainVoyager 20.6 (Brain Innovation B.V., Maastricht, Netherlands). For the MREG data an additional dynamic off resonance correction (DORK (Pfeuffer et al., 2002); using MATLAB (the MathWorks, Natick, MA) was performed. A temporal high-pass filter of three cycles per time course was applied. The high-pass filtering was performed on the native data before the transformation to Montreal Neurological Institute (MNI) space to remove low frequency drifts from the data. In addition, linear trends were removed. No spatial smoothing was applied.

Vascular and anatomical data were collected in a separate session for participants P02, P05, P07, P08, P09 from a 3T scanner (PRISMA fit, MR_VE11C, Siemens Healthcare, Erlangen, Germany) using 2D- and 3D-Time-Of-Flight (TOF; FA = 60°/18°, TR = 21 ms/20 ms, TE = 4.83/3.3 ms, 0.7 mm isotropic resolution) and MPRAGE sequences, respectively (TR = 2250 ms, TE = 2.21 ms, FA = 9°, number of slices = 192, 1 mm isotropic resolution).

### 2.4. MREG co-registration

Unlike MREG, GRE data is relatively easy to co-register to individual anatomical datasets. For this reason, we first acquire a brief GRE reference scan shortly before MREG data is acquired and co-register GRE data to the anatomical dataset. Due to the temporal proximity of both MREG and GRE scans, the resulting transformation matrix can be then used on the MREG data.

More specifically, first the GRE data was stored as a fMRI (fmr) dataset in BrainVoyager. This format allows automatic boundary based registration (BBR) (Greve and Fischl, 2009) of the functional and anatomical reference. Using this automatic procedure all GRE datasets were mapped to each subject's individual anatomical dataset in native space. After co-registration of the GRE images, the resulting transformation parameters were used to map the MREG data to the anatomical image. After transforming the MREG data into MNI standard space, the functional coverage was verified by overlaying all functional runs of all twelve participants on top of the MNI Colin27 standard template (Holmes et al., 1998). We also applied the BBR corregistration procedure to the SMS-EPI data to have maximally comparable results. The quality of the latter was also verified using the method described above, i.e., transforming the data into the MNI space and overlay all functional runs on top of the MNI Colin27 standard template.

### 2.5. General linear model analysis

fMRI data is most commonly analyzed using a general linear model (GLM; (Fadili et al., 2003). To ensure correct GLM analysis of the MREG data, global assumptions of model and noise (e.g., independence of repeated measurements over time (Barker et al., 2013)) were re-evaluated. Since both sequences measured BOLD-related signals, we further investigate only the possibly violated assumptions that were caused by the higher sampling rate of MREG (Hao et al., 2017; Uga et al., 2014).

One assumption of the GLM is that there is no autocorrelation in the residuals (Eklund et al., 2011). However previous work has shown that, this assumption is not always met (K. J. Friston et al., 2000). There are different sources causing the temporal autocorrelation in fMRI, e.g.,

trends, scanner imperfections or physiological noise (Boynton et al., 1996; Eklund et al., 2011). As for the latter, since heartbeat and respiration are clearly visible in the MREG data, we were able to model them as confounds. The beta estimates are not directly affected by autocorrelation, but the serial correlation can result in biased estimates of the error variance and this can lead to inflated test statistic (Tak and Ye, 2014).

To remove these correlations, the fMRI time series needs to be preprocessed. Here, we only focus on one of the most common processes, namely the pre-whitening, which should also perform best in block based stimuli paradigms (Friman and Westin, 2005). To whiten the residuals, multiple steps need to be performed and different models can be used for the pre-whitening method, like auto-regressive (AR), moving-average (MA) or auto-regressive-moving-average models (ARMA, ARIMA or "Box-Jenkins") (Locascio et al., 1997). As the AR model is very often used in fMRI analysis, we decided to use this method (Rogers et al., 2010).

Due to the high sampling rate of MREG data, higher order AR models may be required to sufficiently remove autocorrelation from the residuals. The AR model of a higher order $p$ can be described as:

$$x(t) = \alpha_1 x(t-1) + \ldots + \alpha_p x(t-p) + e(t)$$

The parameter $e(t)$ is the white noise and parameters $\alpha_1, \ldots, \alpha_p$ are the AR parameters to be estimated for the different model orders (Eklund et al., 2011).

A model order needs to be selected objectively. This was done by selecting the model that minimizes an information criterion function. The Bayesian information criterion was used in this study:

$$BIC(P) = -2\,LL + P\,ln(n)$$

The BIC consists of the following parts: P is the model order; LL is the log-likelihood of the model fit; and n is the number of time points (Barker et al., 2013). It has been shown that this criterion worked well for fNIRS analysis (Barker et al., 2016; Uga et al., 2014) which has a similar temporal resolution as MREG.

After the selection of the AR(p) order the AR parameters was estimated using Burg's maximum entropy method. Although very often used, we decided not to use the Yule-Walker approach because it may lead to incorrect parameter estimates in case of nearly periodic signals. Instead, we used Burg's method (Burg, 1975; De Hoon, Van Der Hagen, Schoonewelle and Van Dam, 1996; Kay and Marple, 1981), which is a recursive algorithm aiming to finding a sequence of values so that it constitutes the (empirical) partial autocorrelation function that is also described as reflection coefficients (Pollock and Green, 1999).

The estimated AR parameters are then used to whiten the time series and model predictors using the following equation (Eklund et al., 2011):

$$w(t) = x(t) - \sum_{i=1}^{p} \widehat{\alpha}_i x(t-i)$$

Here p is the order of the AR model and $\widehat{\alpha}_i$ are the model parameter estimates.

To further investigate the relation to the explained variance in the model we conducted GLM analysis with and without additional confound predictors. More details about the added confounds can be found in the following section.

#### 2.5.1. Adding confound predictors using independent component analysis

A suitable tool to improve the GLM model is to add additional predictors which only explain non-task relevant information of the data, so called confound predictors. These predictors can be generated using mathematical models or by extracting information from the data itself, provided that it is not part of the underlying paradigm used in the study.

The BOLD fMRI signal arises from a complex mixture of neuronal, metabolic and vascular processes, and it is further corrupted by multiple non-neuronal fluctuations of instrumental, physiological (including motion) and subject-specific (psychophysiological) origin. Particularly,

motion-related and physiological noise fluctuations are the main noise components of the signal, and data-driven multivariate approaches, such as principal and independent component analysis (PCA and ICA, respectively), strongly benefit from the information available in the shared task-independent phases of multi-voxel time courses. This in turn allows to robustly separate the spatially structured (noise) components from the data sets. After the extraction, the components need to be first classified as either signal or noise, thereby, a denoised fMRI time-series is usually reconstructed based only on the independent components classified as signal.

As a viable alternative, here we used ICA to create and add confound predictors to the GLM, in a sort of hybrid GLM-ICA analysis (see, e. g., (McKeown et al., 1998).,). This was done by first running the FastICA algorithm (Hyvärinen, 1999) on a given fMRI data set as implemented in BrainVoyager (ICA plugin), and then selecting the component time courses as candidate confounds for the GLM. When applied to the multivariate fMRI time-series, the FastICA algorithm allows to extract (up to) a predefined number of independent components, which can then be classified as either task-related or non-task-related signal sources (De Martino et al., 2007; McKeown et al., 1998) according to the correlation coefficient with the GLM task predictors. As we were only interested in non-task-related components, which do not (or only minimally) explain the multivariate (co)variance according to the experimental paradigm, each ICA component time course was correlated with the task predictor time courses and was only selected as a confound predictor in the GLM if the absolute value of the correlation coefficient was below the mean absolute correlation of all components or lower than 0.2. Given the high temporal dimensionality of the MREG time-series, up to 30 ICA components were extracted from each run of each participant using the deflation version (i.e., one by one) of the FastICA algorithm, both for the SMS-EPI and MREG sequence. This approach ensured the computational feasibility of the procedure, even for future real-time applications (see, e. g., (Lührs et al., 2017).,), because spatial maps are not used for reconstruction and the selected confound predictors are by definition not correlated to the GLM predictors (see, e. g., (McKeown, 2000; McKeown et al., 2003). To verify that the extracted components included heartbeat and respiration signal information, it was correlated to the acquired physiological data using the fingertip pulse plethysmograph and respiratory belt. Additionally, for participant P02, P05, P07, P08 and P09, the respiration and pulse components were combined with the pial vessels reconstructed from the time of flight sequence. Only the passive viewing data was used in this analysis step and the number of ICA components was limited to 30 in this analysis subset. First, 2D and 3D TOF data were aligned individually to an up sampled version (0.7 mm isotropic resolution) of the anatomical data of the same session for each participant. Vascular data were segmented using a two-stage approach: the first stage involved using automatic segmentation tools in Brainvoyager QX v3.2 (intensity-based segmentation) and Segmentator (intensity gradient based segmentation) (Gulban and Schneider, 2016) and a second step focused on polishing the resulting segmentations manually. The segmented vascular structures from 2D and 3D TOF data were then combined in one dataset and were down sampled to 1 mm isotropic resolution. To show that the selected components for pulse and respiration are not only correlated with the heartbeat and respiration signal the individual pulse and respiration component maps were masked with each individual vessel reconstruction. The components were automatically selected by correlating them with the pulse and respiration signal recorded during the measurement. Afterword's the component with the highest correlation was chosen as a reference and all components having a correlation within one standard deviation apart from the maximum correlation. To test the spatial properties of the components all selected pulse and respiration components were combined into one map and masked with the vessel reconstruction. The same procedure was applied to the task relevant components. Afterwards the combined number of voxels in the ICA pulse and respiration maps were compared to the amount of voxel in the task component, also after masking with the vessel

reconstruction.

### 2.6. Temporal signal to noise comparison

To compare the overall signal quality, we conducted a comparison of the signal-to-noise ratio of the SMS-EPI and MREG data. This ratio can be seen as a comparison of the global signal level related to noise were the global signal is comprised of baseline and activation periods (Murphy et al., 2007; Welvaert and Rosseel, 2013). This gives an indication of the overall signal quality compared to the background noise. Additionally, temporal filtering was applied using Gaussian full width half maximum kernel of 2s low pass filter. This way the cleaned time course only consisted of the information of interest. Because this also inflates the noise term correlations of the GLM, we applied the filtering only to run a tSNR comparison between MREG and SMS-EPI data. The following equation was used:

$$tSNR = \frac{\overline{S}}{\sigma_N}$$

where $\overline{S}$ is the average voxel time course and $\sigma_N$ the standard error of the mean.

The resulting tSNR maps contain a statistical difference between all SMS-EPI runs of all twelve participants compared to all MREG runs of all participants further described in the results section. For MREG data, tSNR values were computed using filtered and unfiltered data in order to see the effects of temporal filtering on the MREG data containing physiological information. This was also done for the SMS-EPI (400 ms TR, MB 8).

### 2.7. Functional connectivity analysis

We investigated the potential benefits for functional connectivity analysis of a sequence with higher temporal resolution using both, simulated and real data (Akin et al., 2017). For the former, a partial correlation between two simulated time courses was modeled first. This was done using a double gamma hemodynamic response functions (HRF) (Glover, 1999) and convolving it with a box car function according to the block design protocol. Then, white noise was added to mimic a fMRI signal, resulting in an SNR of the simulated time course of ∼ -3 db. A control region was formed by only a white noise signal with zero mean. The partial correlation of two simulated time courses controlled for the white noise only signal was repeated 1000 times to model the difference in connectivity shape. This step was performed using (1) a temporal resolution of 2s simulating the SMS-EPI repetition time; (2) a temporal resolution of 100 ms simulating the MREG sampling rate. This simulation focuses on the differences in temporal resolution and points out the direct effect of a sampling rate. The results of this analysis can be found in section 3.4. To verify the results of the simulated data we also extracted time course information from the motor imagery experiment of all participants. We selected left sensorimotor (LSM) and left premotor (LPM) areas based on the SMS-EPI and MREG Stroop experiment run respectively and used a control region in white matter to control for global noise and physiological artifacts using the partial correlation analysis. Selecting the region in a different run is important to avoid misleading statistics caused by double dipping. The analysis should show the difference in partial correlation between LSM and LPM controlling for general signal fluctuations using a white matter ROI between the MREG and SMS-EPI sequence.

### 2.8. Temporal down sampling of MREG to EPI resolution

To be able to compare both signals in a direct application as a signal source for NF applications, the MREG time course was down sampled to the temporal resolution used for the SMS-EPI sequence (2s). Down sampling was applied to create data as close as possible to hypothetically

acquired data which are also only snapshots of specific time points. The down sampling was performed by decreasing the sample rate of the MREG data by keeping the first sample and then every 20th sample after the first. Similar to the functional connectivity analysis the time course of LPM was extracted in both MREG and SMS-EPI for all participants in the motor imagery experiments.

## 3. Results

Since real-time reconstruction of MREG signal yields to virtually identical signal (i.e., the magnitude sums over the ROIs), as compared to the standard reconstruction (Riemenschneider et al., 2019), only offline reconstructed data was used in this manuscript.

### 3.1. GLM and ICA analysis

The GLM results mainly focus on the estimated AR model orders and the effect of adding additional confound predictors using ICA.

#### 3.1.1. ICA confound predictors
ICA was used to obtain additional confound predictors that were added to the GLM analysis. As shown in Fig. 2 the respective ICA components for respiration and cardiac pulsation significantly correlated with the recorded cardiac pulsation and respiration data. For example, the respiration data for participant P07 gave a Pearson correlation of $r = 0.4943$ with the respective ICA component. After filtering (lowpass 0.7hz) the correlation increased to $r = 0.87$. Looking at heartbeat a Pearson correlation of $r = 0.89$ for the specific ICA component was found. Both were significant ($p < 0.001$).

Fig. 2 depicts the ICA component maps for cardiac pulsation (red) and respiration (blue), as well as their respective time course are shown, together with the respective reference time course of the respiratory belt and fingertip pulse plethysmograph.

For the subset of participants were an additional vessel reconstruction was available the mean Pearson correlation were $r = 0.67$ for respiration compared to the respective ICA component and for the heartbeat an average Pearson correlation of $r = 0.71$ with the specific ICA component was achieved, both being significant ($p < 0.001$). A detailed plot of the single correlations and picked components is shown in Fig. 3. On average 3.8 components were selected from the pulsation correlation and 1.4 from the respiration signal correlation.

The comparison of the voxel count after masking with the vessel reconstruction showed a median of 563 voxels (min 524, max 708) for the combination of the pulse and respiration components and a median of 387 voxels (min 220, max 400) for the passive viewing task component. The difference was significant ($p < 0.005$). A detailed boxcar representation is shown in Fig. 4.

#### 3.1.2. GLM AR orders
For all MREG experiments, BIC analysis estimated an average AR order across runs and participants of 21.30 without incorporating the ICA confound predictors. If the confound predictors were incorporated the estimated AR order was reduced to 17.97 (1.798s). Fig. 6 depicts the Bayesian information criteria for participant P05 of all three experiments using the MREG sequence.

Comparing individual AR order maps of each voxel for all participants showed a significant decrease of the estimated autocorrelation order ($p < 0.05$) in 61.32% of all voxels and a t-value below 0 (comparing MREG including ICA confound > MREG without confounds) in 97.8%.

To illustrate the effect of the statistical inflation using no or low models for the autocorrelation correction, different AR models were used. Statistical maps for the motor imagery task are presented for subject P04 in Fig. 7.

As shown in Fig. 7A, no additional confound predictors were used and only the t-statistics of motor-imagery vs. rest are presented (Bonferroni corrected at $p_{bonf} < 0.0001$) using different AR orders (0, 2, 20) (0s, 0.2s, 2.0s). Fig. 7B shows additional ICA confound predictors were added and the t-statistics of the contrast motor-imagery > rest is shown (Bonferroni corrected at $p_{bonf} < 0.0001$) for different AR orders (0,2,18) (0s, 0.2s, 1.8s). The high AR orders (20 and 18) (2.0s, 1.8s) differ because they were estimated using BIC. Although, in individual participants this decrease is not significant ($p > 0.05$) across individual voxels. At the bottom of Fig. 6, the SMS-EPI analysis results are shown using a standard AR (2) model, with (B) and without ICA confound predictors (A). Unlike for SMS-EPI data, MREG data shows an increase in t-statistics when adding additional confound predictors. To show this effect in a specific
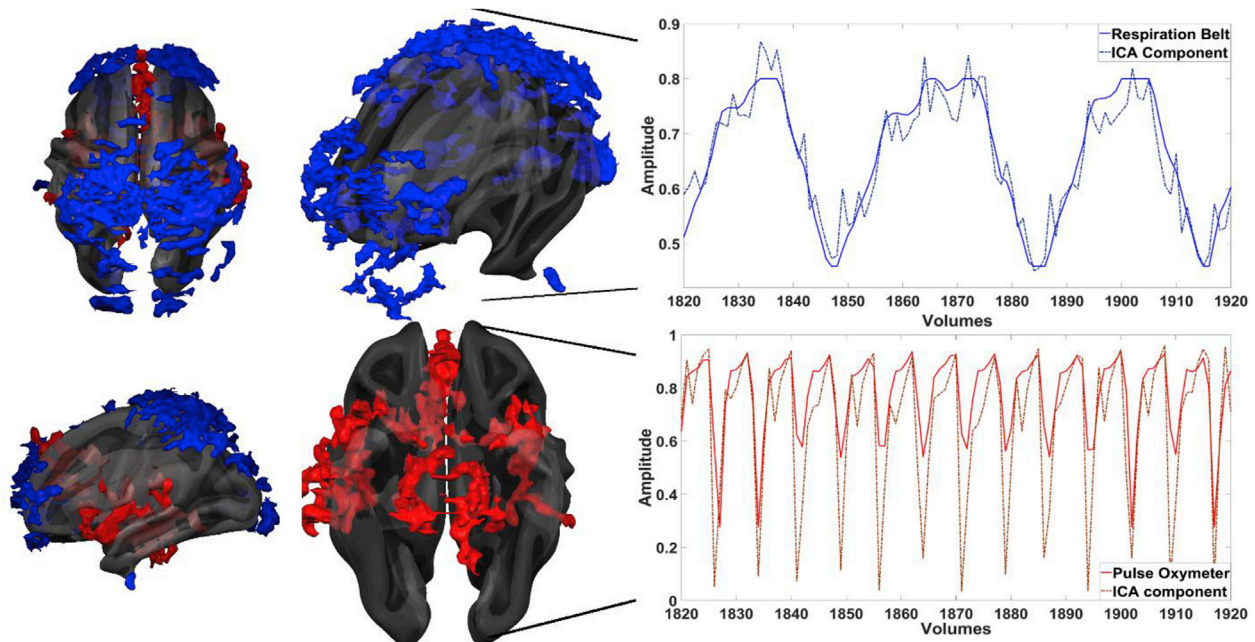


**Fig. 2.** ICA components for respiration (top) and cardiac pulsation (bottom). On the left side the respective IC-maps are shown. Respiration is presented in blue and cardiac pulsation in red. On the right one can see the respective time course for the heartbeat (bottom) and respiration (top) component both drawn in blue. The red time course represents the recorded heartbeat and respiration using pulse plethysmograph and respiration belt respectively.
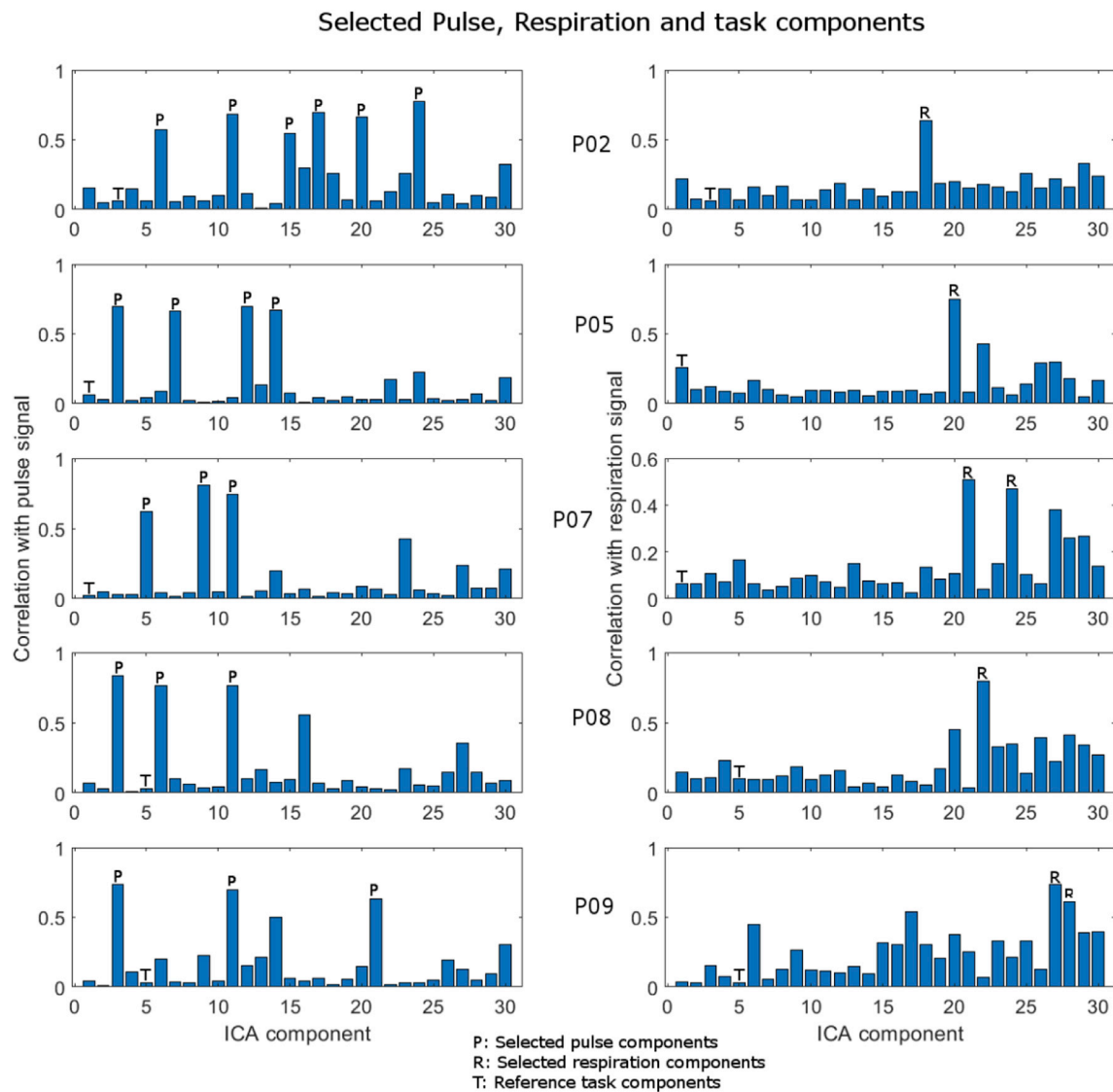
## Selected Pulse, Respiration and task components



**Fig. 3.** ICA components correlated against recorded cardiac pulsation signal (left) and respiration (right). The letter "P" on top of a correlation bar points out the selected pulsation component. The letter "R" on top of a correlation bar shows the selected respiration component. As a reference the component with the highest correlation to the passive viewing task is indicated by a "T" on top of the correlation bar.

volume of interest, we performed a ROI GLM analysis on the motor imagery run of P07 (10 mm radius cube centered at MNI coordinate: 6, −5, 57; Right BA 6, primary motor cortex). For MREG, the explained variance increased from 50.84% to 72.76%. This effect was smaller for SMS-EPI data, which increased from 63.20% to 71.74%. Here the t-values decreased when adding the ICA confound predictors to the GLM. Overall the decrease in statistical inflation using higher AR(p) orders can clearly be seen when looking at the different t-maps. The t-values for SMS-EPI and MREG data were both Bonferroni corrected ($p_{bonf} < 0.0001$).

A detailed time course plot of the selected ROI is shown in Fig. 8 which includes the model and error terms, as well as autocorrelation functions (ACF) for no AR correction and AR (2) correction. The ACF of the residuals using the estimated AR based on BIC was a nearly flat line and therefore not included in the plot because of no visible differences in the lags of the ACF.

The explained variance of the GLM significantly increased ($p < 0.001$) for both the SMS-EPI and MREG sequence when ICA confound predictors were included. On average the explained variance increased from 26.91% to 48.42% for the SMS-EPI sequences and from 26.37% to 51.30% for MREG sequence. There was no significant difference between the increase of the SMS-EPI and MREG sequences. A detailed plot of all

runs and the individual $R^2$ is presented in Fig. 9.

### 3.2. RFX analysis

The RFX analysis revealed an overall consistency of SMS-EPI and MREG data. The comparison of the t-statistic of each map was based on Spearman RHO (Kornbrot, 2014). For the motor imagery run RHO was 0.4469, for passive viewing 0.4762 and for the response (Stroop) task 0.4910, all three of them were significant at $p < 0.01$. An overview of the individual maps is shown in Fig. 10.

Even though the correlation results are not significantly different, the overall overlap between the different experiments is diverse. As for the motor imagery paradigm the overlap is quite consistent and only differed minimally with a higher statistical power for the MREG data. The overlap is comparable to the passive viewing paradigm with the difference of a higher statistical power in the SMS-EPI data. Whereas in the STROOP task we found a much stronger statistical power and a wider spread activity in the SMS-EPI as compared to the MREG data. Differences in the point spread function (PSF) of the SMS-EPI and the MREG sequences show potential explanations especially in the sinus frontalis and the temporal nodes (Assländer et al., 2013; L. Chen et al., 2015).
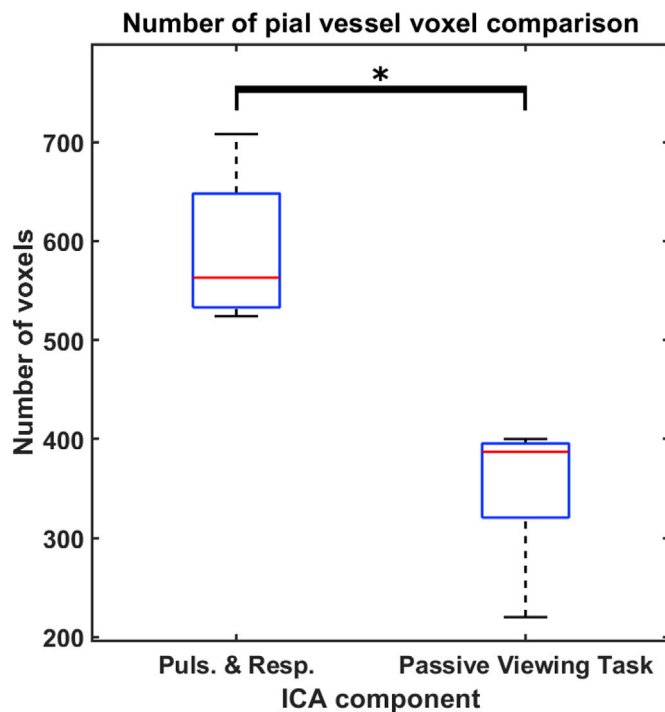
## Number of pial vessel voxel comparison



**Fig. 4.** Box plot of the number of pial vessel voxel of pulse and respiration components (left) compared to the passive viewing task component (right). The difference was significant ($p < 0.005$). The absolute average of all selected pulse and respiration IC-maps masked with each individual vessel reconstruction was descriptively compared to the average vasculature data in Fig. 5.

### 3.3. tSNR

The tSNR maps were compared using a pairwise *t*-test of the SMS-EPI and MREG runs (motor imagery, passive viewing, Stroop task) for each participant. The results are shown in Fig. 11. Fig. 11 left shows the SMS-EPI runs compared to the unfiltered MREG runs whereas Fig. 11 right shows the filtered SMS-EPI runs compared to the filtered MREG runs using temporal smoothing with a gaussian kernel FWHM of 2s.

Primary and supplementary motor areas as well as the ventrolateral prefrontal cortex, dorsal anterior cingulate and inferior temporal cortex show significantly higher tSNR for SMS-EPI compared to the unfiltered MREG runs ($p < 0.05$ Bonferroni corrected). After temporal filtering (Fig. 11 right) the Primary and supplementary motor areas don't show any difference in tSNR, whereas the difference is maintained in parts of the dorsal anterior cingulate and the inferior temporal cortex.
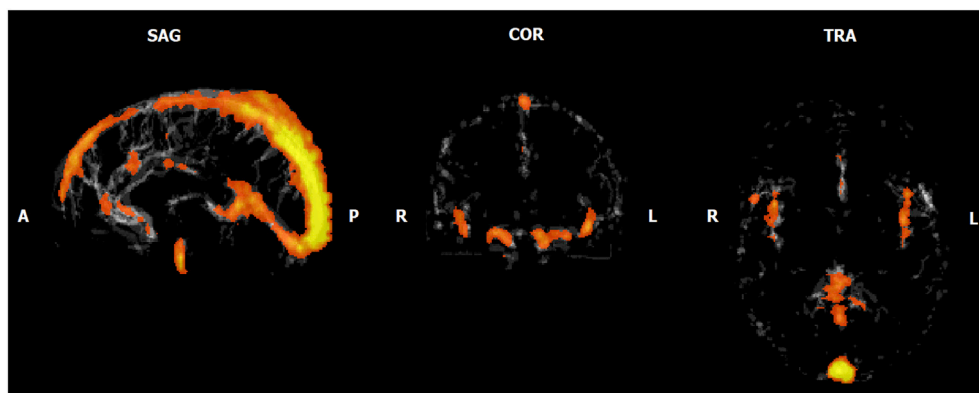
### 3.4. Functional connectivity

The partial correlation of the generated white noise time courses convolved with the HRF (green time course in Fig. 12) showed lower standard deviation for the high sampling rate (100 ms sampling, blue time course) compared to the low temporal resolution (2s sampling, red time course). The 2-s sampling was up-sampled to display the results in one graph. On the left side of Fig. 11 a correlation window of 20s was used and on the right-hand side, a correlation window of 32s was used. The blue curve (100-ms sampling) shows a lower standard deviation compared to the red curve (2s sampling), which was significant at $p < 0.01$. This finding was true for the short (10s) and long (20s) window (see left and right upper part of Fig. 12). We also found this effect for the SMS-EPI (green curve) and MREG data (blue curve). High sampling MREG data showed significant lower standard deviation in the partial correlation ($p < 0.01$) for both for the short (10s) and long (20s) window (see C) and D) in Fig. 12).

### 3.5. Temporal down sampling of MREG to SMS-EPI resolution

The down sampled MREG time course (to match the SMS-EPI temporal resolution) resulted in a significantly lower variance compared to the SMS-EPI ($p < 0.05$). As an example, a motor imagery trial with both time courses is shown in Fig. 13.
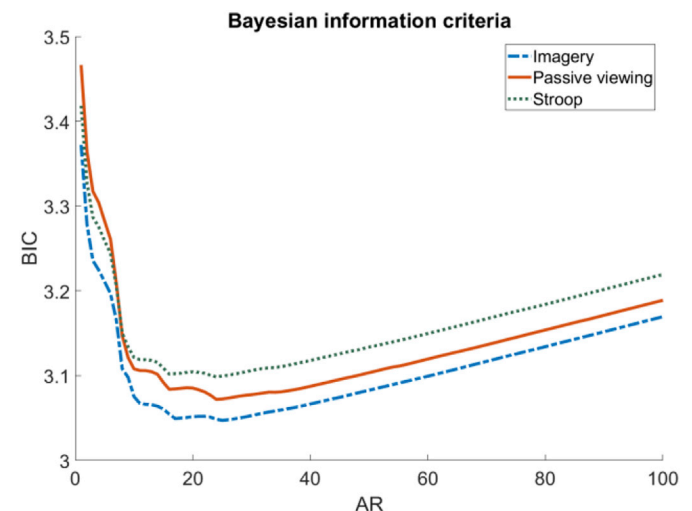


**Fig. 6.** Bayesian information criteria and AR order. Based on the three different runs (Imagery, Passive viewing, Stroop) of participant P05. BIC against AR order was average across all brain voxels were.



**Fig. 5.** Average absolute pulse and respiration components overlaid on top of the average pial vessel reconstruction of the described participants subset. Individual pulse and respiration components were masked with the subjects individual TOF reconstruction and afterwards averaged.
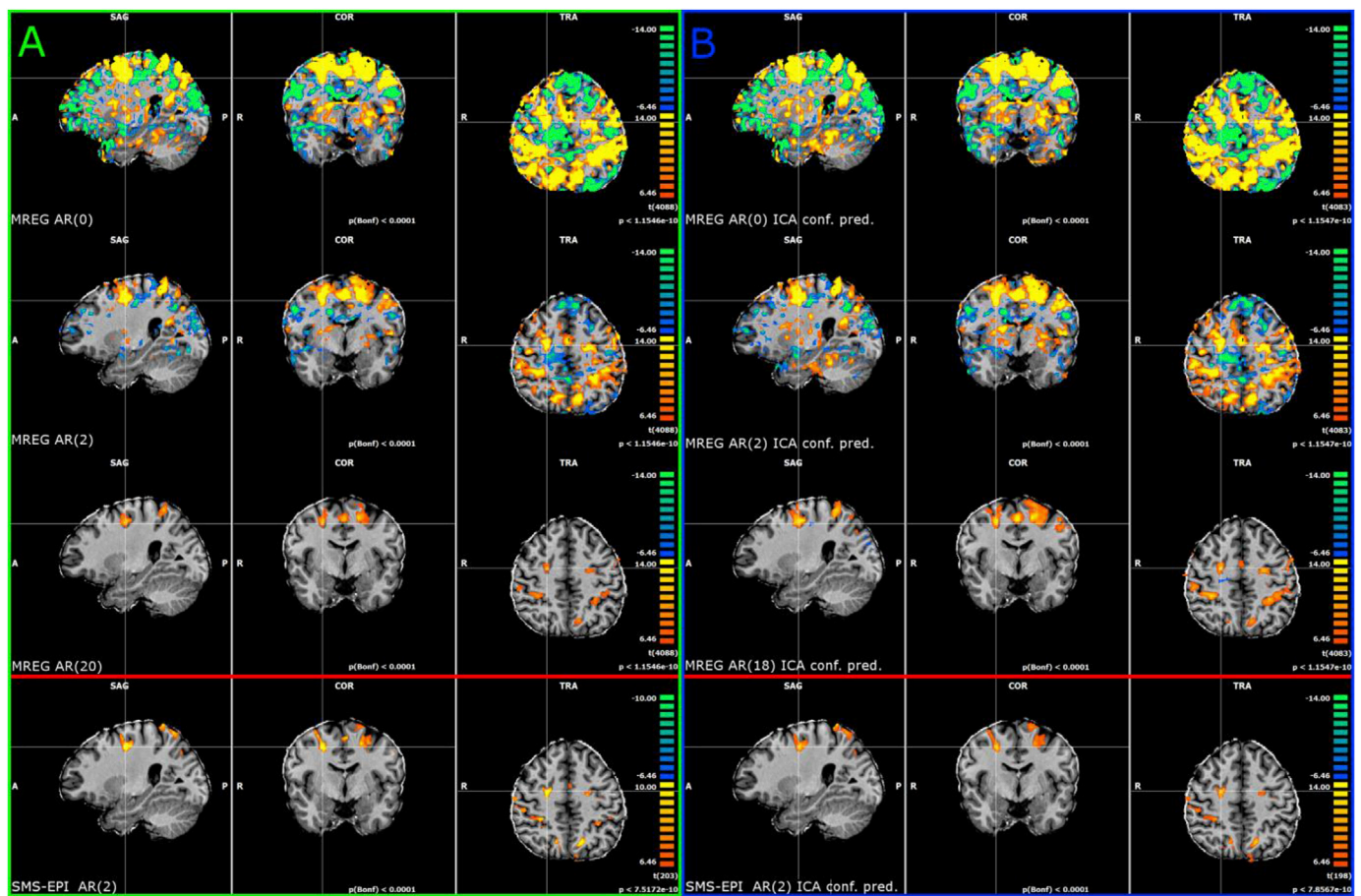
**Fig. 7.** MREG AR correction using different AR orders. A) AR correction of standard GLM residuals without additional confound predictors (only motor imagery > rest). Different orders were used to investigate the effect of proper AR correction. The higher the order the lower the calculated t-values. B) AR correction of GLM including additional confound predictors for heartbeat and respiration extracted using ICA. The t-values are overall higher compared to the maps shown in part A. In the bottom of the figure a SMS-EPI analysis result is shown as a reference, once with (B) and once without (A) additional ICA based confound predictors.

### 3.6. Comparison to higher order multiband SMS-EPI

One participant (P07) was additionally scanned in a separate session using the SMS-EPI sequence described earlier with adjusted scanning parameters: 1000 vol, TR/TE = 400 ms/30 ms, flip angle 42°, 3 mm isotropic nominal resolution, matrix size of $64 \times 64 \times 48$ resulting in a $192 \times 192$ mm FOV, multiband factor 8, $48 \times 3.0$-mm slices without gap. This was done to explore whether a higher MB-factor combined with a lower TR of 400 ms allows to separate cardiac and respiratory signal sources. Appendix A. Fig. 1 depicts the resulting ICA component maps of participant P07 for cardiac pulsation (red) and respiration (blue) as well as their respective time courses, in addition to the reference time course of the respiratory belt and fingertip pulse plethysmograph. The selected ICA components showed a Pearson correlation of $r = 0.82$ with the respiration data of participant P07 as well as $r = 0.77$ with the time course of the recorded heartbeat, with both correlation coefficients being highly significant ($p < 0.001$). An overview of the selected independent components for this extra scan can be found in Appendix A, Fig. 2. The tSNR differences between SMS-EPI 400 ms TR, MB 8, and the MREG sequences are shown in Appendix A. Fig. 3. The calculations were the same as described in section 3.3. There was a widespread significant gain in tSNR for MREG as compared to SMS-EPI 400 ms TR, MB8 runs ($p < 0.05$ Bonferroni corrected), encompassing mostly parietal, posterior temporal and occipital regions as well as parts of the frontal lobe. After temporal filtering most of these differences are diminished, leaving only few local spots in the anterior temporal lobe and the cerebellum with increased tSNR for the SMS-EPI sequence.

### 4. Discussion

In this work we investigated the potential benefits of a recently developed parallel imaging technique MREG particularly for a possible use in real-time BCI and NF applications and compared it to a SMS-EPI sequence. Several parts of the analysis pipeline were investigated to point out specific differences in the pre- and post-processing of the fMRI time-series generated by these sequences.

Generally, higher sampling rates (lower TRs) enable more detailed models of the HRF, e.g., for detecting the initial dip (Hu and Yacoub, 2012) and to observe sub-second timing differences in task-based processes. However, higher sampling rates result in lower spatial resolution or brain coverage in non-parallel image acquisitions. It has been shown that higher acceleration factors for SMS-EPI reduce the tSNR (L. Chen et al., 2015). As discussed in a recent paper by Hsu and colleagues (Hsu et al., 2017) the reduction in tSNR with each acceleration factor might be a limiting factor for very low TR's around 100 ms so that SMS-EPI is potentially not suited for the comparison of differences and improvements at a higher temporal resolution (Feinberg and Setsompop, 2013; Hsu et al., 2017). In the additionally scanned dataset using the SMS-EPI with 400 ms TR and MB8 we didn't see this strong limitation as described in the discussion from Hsu and colleagues. Also in a very recent article from Chen and colleagues (J. E. Chen, Polimeni, Bollmann and Glover, 2019) it is suggested that the use of higher multiband factors and lower repetition times using SMS-EPI relies on multiple factors and can't be trivially explained or judged. As shown in Appendix A, Fig. 1, the 400 ms SMS-EPI also allows to disentangle the physiological information from
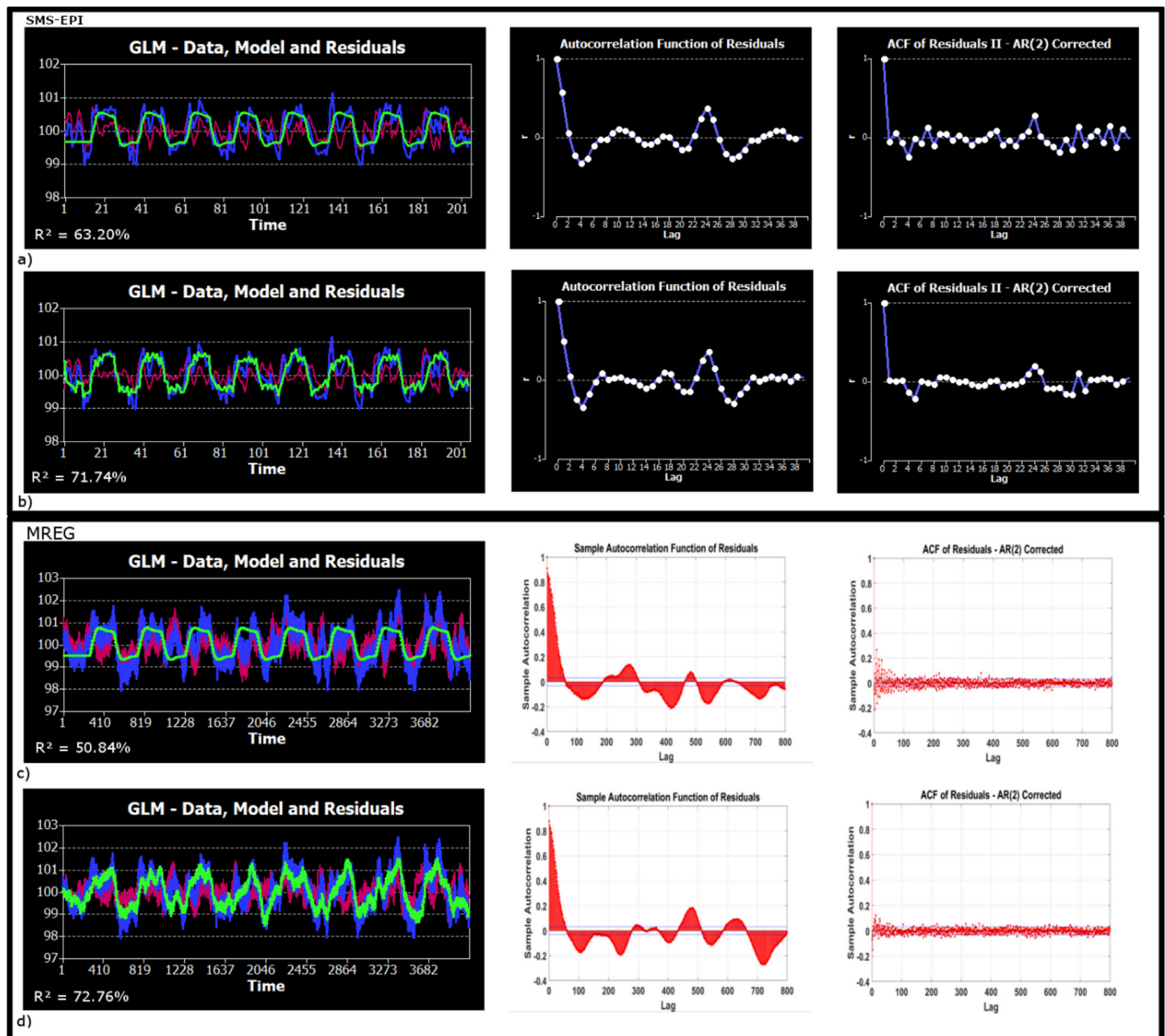
**Fig. 8.** Time courses, models and residuals of an ROI GLM (P07, Motor Imagery). The left part of the figure shows the time course for SMS-EPI (top) and MREG (bottom) The upper plot (a and c) shows the GLM results without additional IC based confound predictors. The lower part (b and d) includes IC based confound predictors. The data is presented in blue, the model in green and in red the residuals (error) of the GLM. In the center the ACF for the residuals of the plot next to is shown. On the right the individual ACF's after AR (2) correction are presented.

the BOLD signal. But it is also clear, that the shape of the heartbeat signal is not as clearly described as shown in Fig. 2 using the MREG sequence with 100 ms TR. This effect could be explained by the higher temporal resolution and allows no judgment of the quality of the two different sequences but clearly shows the potential of high temporal resolutions for these types of physiology. Also, when looking at the individual detected IC components (see appendix A, Fig. 2) the results suggest a similar potential of SMS-EPI using higher temporal resolutions to reveal these components in the fMRI signal. Comparing the tSNR of the SMS-EPI with 400 ms and MB8 and the MREG sequence (see Appendix, Fig. 3), the difference in tSNR is mainly visible in the unfiltered data. Other techniques like inverse imaging (InI) (Lin et al., 2012) or simultaneous multi-slice inverse imaging (SMS-InI) (Hsu et al., 2017) are potentially less affected by the tSNR reduction using higher MB-factors and might be potential alternatives. The depicted structures of the IC components shown in Appendix A, Fig. 1, left hand side, also differs between MREG

and 400 ms SMS-EPI. The respiration component is clearly visible in both sequences (maybe even stronger in the SMS-EPI), whereas the pulse component is very different in both sequences. Suggesting that both, the MREG sequence and the 400 ms SMS-EPI might include additional information. Future studies are warranted to provide a full comparison of MREG with SMS-EPI over a wide range of TR and MB on a larger cohort of subjects and data sets.

Overall the tSNR of the SMS-EPI (2s TR, MB 2) and MREG were comparable after low-pass filtering. For the tSNR the mean of the signal is divided by its standard deviation. Thus, a higher sampling rate which will implicitly include physiological noise in the signal will decrease the tSNR. Since this physiological signal is not clearly visible in the SMS-EPI with 2s TR but smeared through the time series it is necessary to bring both sequences into the same temporal space for a fair comparison. The decision to filter the data instead of down sampling the MREG data was practical decision since we didn't expect huge differences between
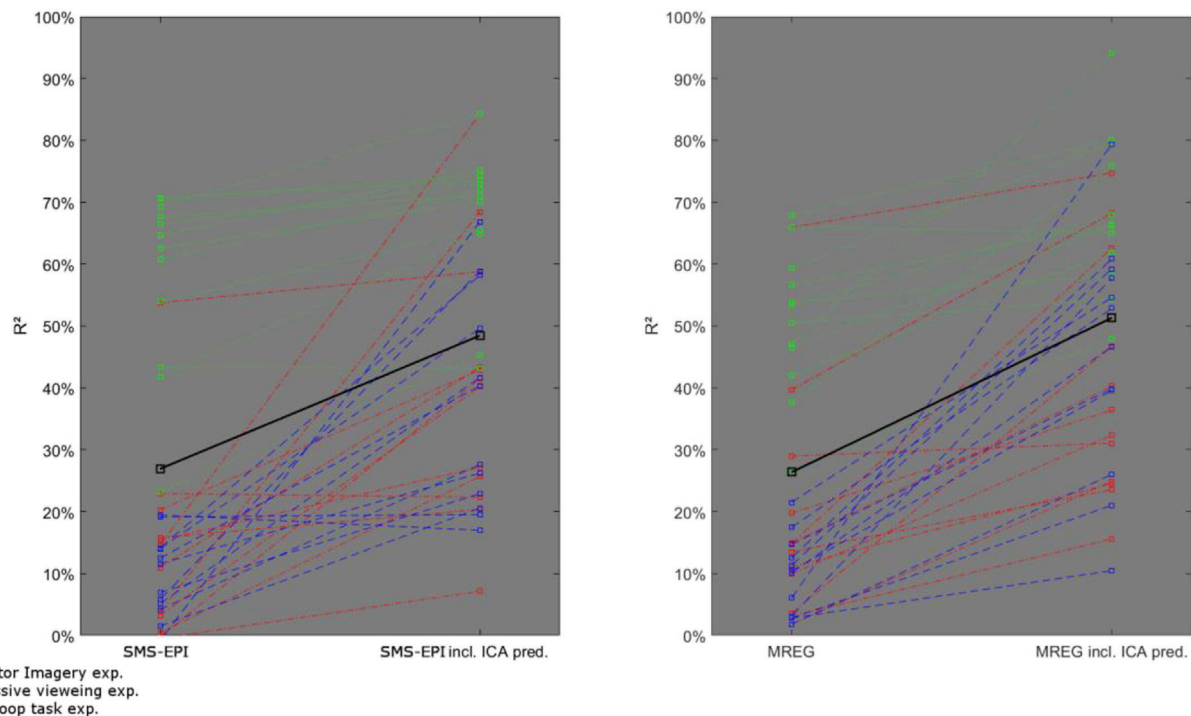
**Fig. 9.** Explained variance of SMS-EPI and MREG ROI GLMs. In the left plot R$^2$ of the SMS-EPI GLM without additional confounds compared to the GLM including ICA confound predictors. On the right the same plot for MREG. Red being the motor imagery runs, green the passive viewing experiments and blue the response (Stroop) task sessions. Three ROI's were selected anatomically for each task.

filtering or down sampling with respect to the tSNR results.

In frontal (above sinus frontalis) and inferior temporal regions a lower tSNR of MREG was present.

Since for most NF applications the signal time course is used as a feedback source, the lower spatial resolution or coverage may be not necessarily a problem especially if the brain areas of interest can be targeted using a spatial resolution of 5–6 mm (or less).

Anyway, these drawbacks potentially resolve over time with the advent of parallel imaging techniques (Akin et al., 2017; Assländer et al., 2013; Hennig et al., 2007; Zahneisen et al., 2011, 2012).

The proposed real-time setup described in the introduction needs two session to first localize the region of interest offline and use this area in the second session for real-time neurofeedback. This seems to be a huge disadvantage compared to other real-time techniques allowing high sampling rates. To overcome this issue the localizer could be shortened to only include two trials of one task or two different tasks (e.g., to perform a contrasting). This was already done by (Nicholson et al., 2017) who included two trials in the beginning of the neurofeedback run to select the 33% best voxels within a predefined anatomical mask with respect to the task or contrast. Combined with a method described in a previous study (Lührs et al., 2017) it would be possible to automatically select this areas within the same session. This could be done since all the steps, from reconstruction to the final region of interest selection can be automatized.

MREG required adjustments to the standard fMRI processing pipeline, mainly, (1) functional/anatomical co-registration accounting for the lower spatial resolution of MREG, (2) adjusted statistical GLM analysis to correct for the higher temporal autocorrelation and (3) temporal filtering adaptations to remove heartbeat and respiration confounding signals. These differences will be discussed in the following sub-sections.

### 4.1. MREG co-registration to anatomical data

A short GRE sequence was used right before the MREG scan was collected and the time between both scans was set to 10s. It was assumed

that during this period the head motion was absent or was very small between. To reduce potential motion in this interval and to keep its duration constant, we informed the participant before the start of the GRE sequence and did not communicate between GRE and MREG to keep the time low in which potential motion can occur. Even though this approach does not completely prohibit the potential of motion-related misalignment, it seemed to be a good starting point and can be improved in following experiments by adding a (e.g., non-linear (Klein et al., 2009); alignment step.

### 4.2. ICA confound predictors

To separate task-related signals from physiological fluctuations of no interest, ICA was used to identify noise components. The number of independent components is still a debate in current literature (Kairov et al., 2017). However, since the overall goal in this case was to only include confound predictors in the model, and not to find task relevant predictors or to spatially model functional networks, the question of the best number of ICA components is less relevant. Particularly, there were at least three reasons for keeping the number of ICA components very low: (i) the risk of losing physiological components is inversely related to the variance contribution of these components; thereby, the higher the contribution of physiological components, the better these will be extracted using relatively less temporal dimensions, whereas the lower the contribution of physiological components the lower the impact of potentially missing these components as confounds in the GLM; (ii) if two physiological components are not well separated (spatially) the removal of the (mixed) effects will operate as one, instead of two, confound predictors; (iii) the residual presence of task-related variance in a physiological component will be controlled by the increased correlation with the task predictor.

Apart from these qualitative expectations, we still checked for each participant that we found (at least) one heartbeat and one respiration component which were of most interest in this study. Indeed, the current results show that even when only using a few components, clear patterns
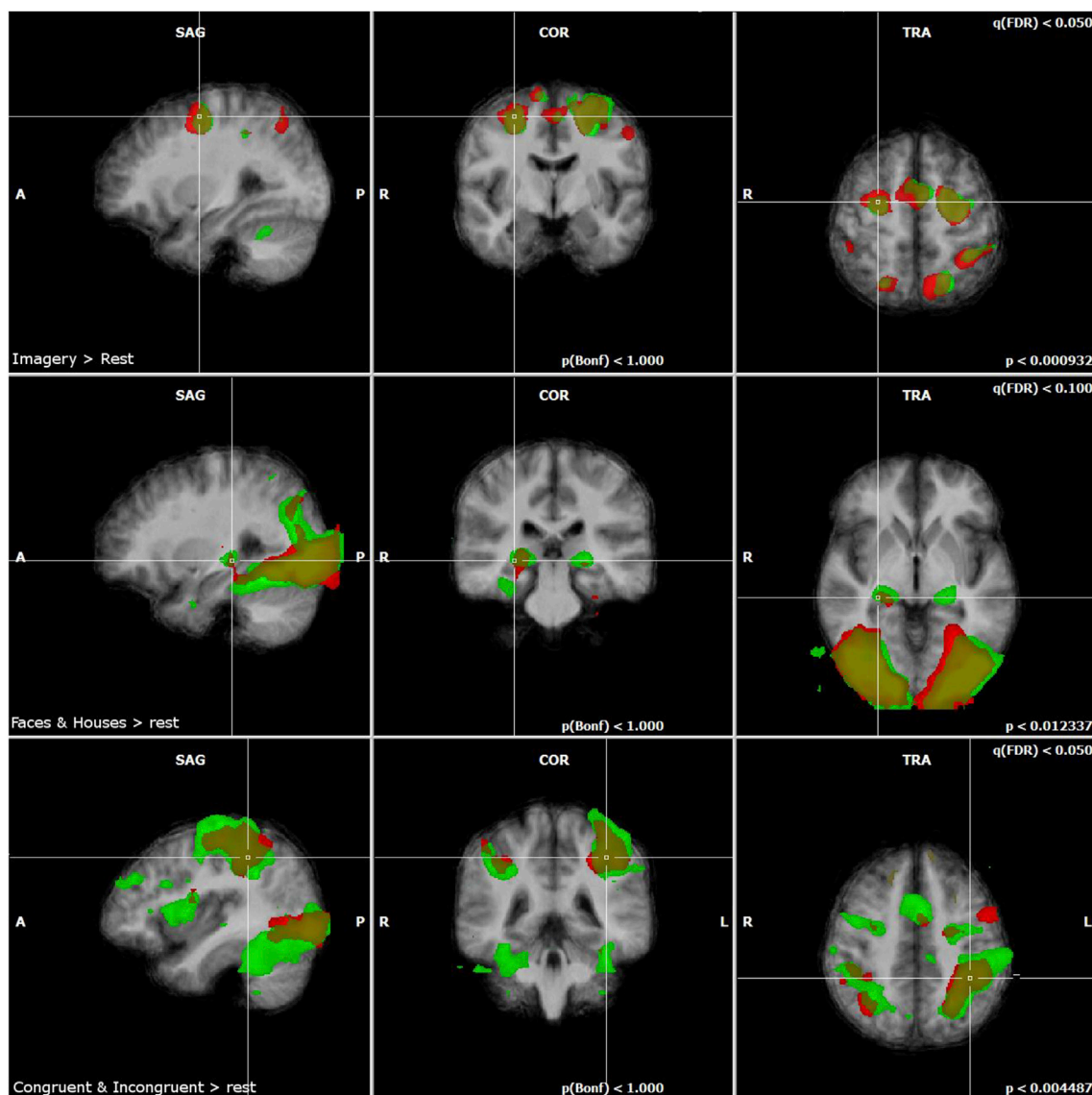
**Fig. 10.** t-statistics of RFX GLM's comparing SMS-EPI (green) and MREG (red). Top part show RFX results for the motor imagery paradigm (imagery > rest). In the center the passive viewing experiment is shown (faces & houses > rest) and in the bottom the Stroop task (congruent & incongruent > rest).
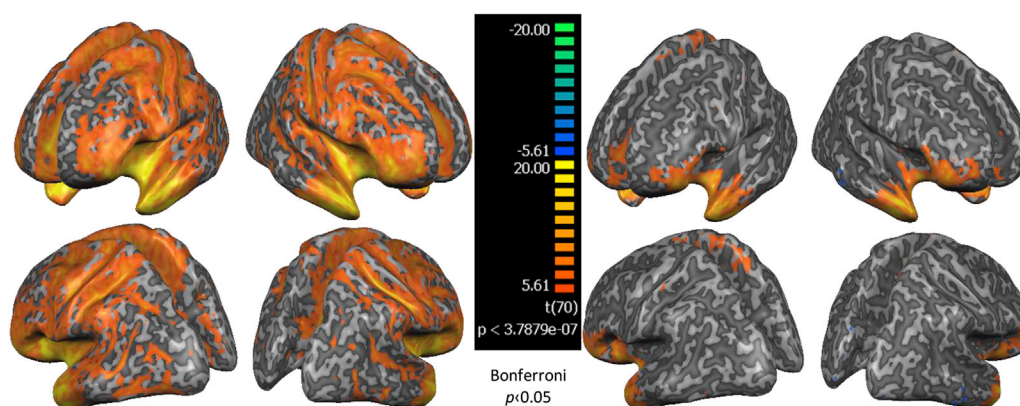


**Fig. 11.** tSNR t-maps for SMS-EPI > MREG. The left side of the figure shows the *t*-test of SMS-EPI > MREG. On the right the same *t*-test is shown with an added temporal low pass filter for the MREG sequence. The maps are Bonferroni corrected ($p_{bonf} < 0.05$).

for cardiac pulsation and respiration are quickly selected, as indicated in Fig. 2. Interestingly, we were able to discern arterial structures like the circle of Willis when mapping these specific ICA confound components

from the MREG data. As for the respiration component, a clear superficial pattern of the component map was visible. The further analysis of the vessel reconstructions from a subset of participants showed the further
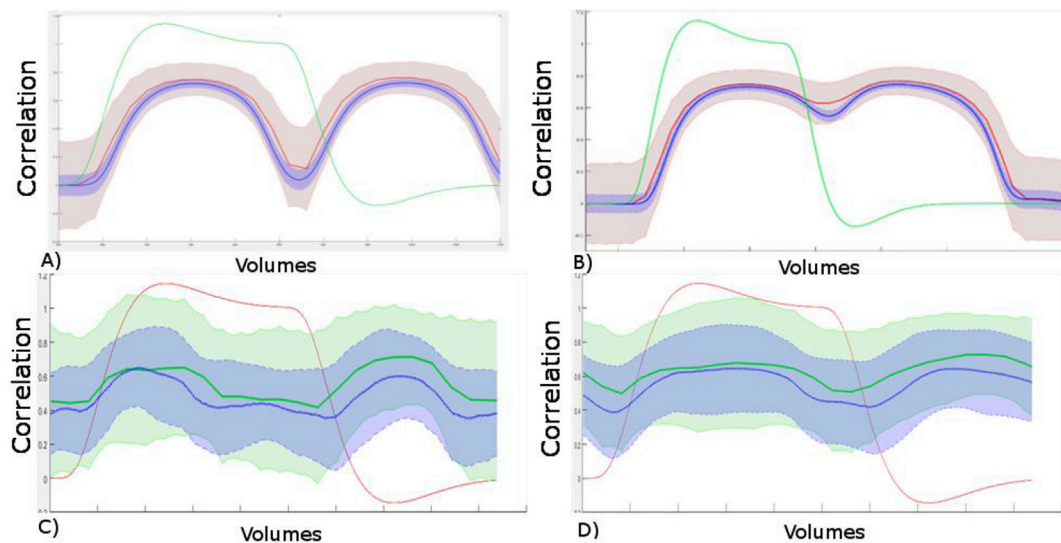
**Fig. 12.** Functional connectivity analysis using partial correlation. Top: simulated partial correlation for A) 10s moving window and B) 20s moving window. The partial correlation consisted of two double gamma HRF with added white noise controlled for an only white noise time course. Red curve, 2s sampling, blue curve 100 ms sampling (the red curve was up sampled to match the plot). Bottom: partial correlation of LSM and LPM (controlled by using a white matter ROI) in SMS-EPI (green curve) and MREG (blue curve) for C) 10s and D) 20s. In red and green, as a reference, the standard double gamma HRF is depicted.
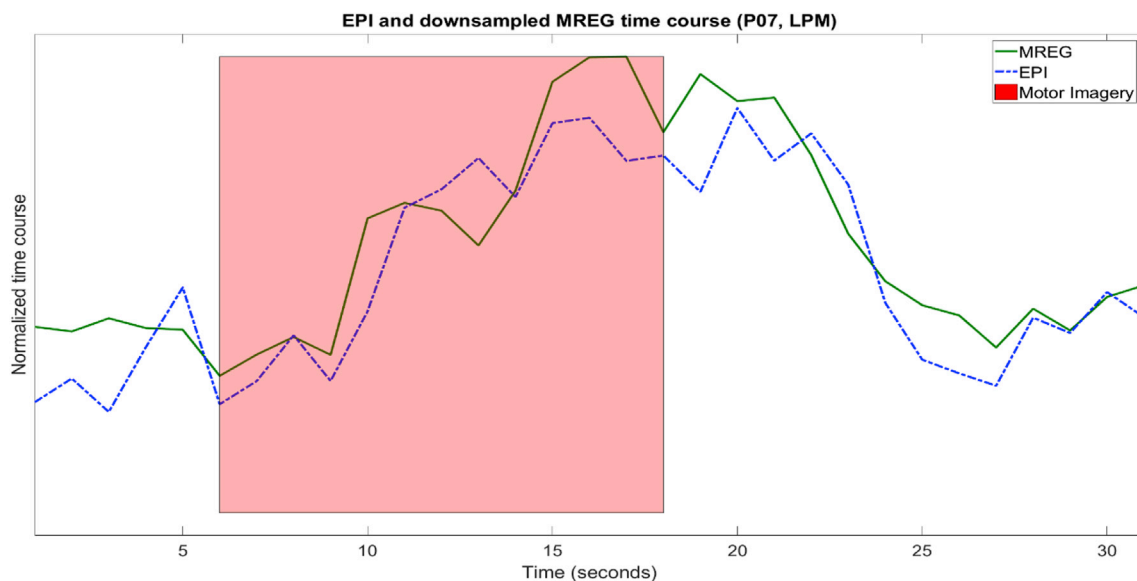


**Fig. 13.** Down sampled MREG time course compared to the standard 2s TR SMS-EPI sequence. MREG time course has significant less variance compared to the SMS-EPI time course ($P < 0.05$).

potential of high sampling rates for fMRI data analysis. We could show that when using more independent components in this subset analysis (30 components) that multiple components were present which covered the pulse and respiration signal. We found on average more components for the pulse signal compared to the respiration signal. This could have been cause by the slice positioning which may not covered the superficial layers in all participants properly. Furthermore, we could show that the selected components shared more voxels with the reconstructed vessels compared to the found task component. This, in combination with the overall very high correlation of the ICA component time courses should be enough evidence that it is possible to extract pulse and respiration information directly from the MREG signal. For the pulse components we could see very often a clear temporal high frequency noise (tHFN) pattern as described by (De Martino et al., 2007). As they also reported that the tHFN was consistently represented across the runs with a clear fingerprint. Since we could now show the source of this component the noise

part might be replaced by physiology, temporal high frequency physiology (tHFP). Being able to clearly reconstruct the pulse and respiration signal the use of RETROICOR might be not necessary for this high sampling rates.

This is particularly encouraging for real-time BCI applications in which it is very important to control for respiration artifacts to ensure that participants did not achieve to reach a certain NF goal only by changing the respiration rate. Using MREG this could be implicitly controlled extracting the ICA component even without acquiring additional respiration information using a respiration belt. Nevertheless, further investigation is needed to further improve the selection of confound predictors especially for SMS-EPI and MREG studies using a very high sampling rate, and possibly build more abstract and general models to correct for physiological artifacts, eventually including spatial information. Such investigations will likely benefit from the use of several ICA component features (see, e. g., De Martino et al., 2007) that,

besides the task correlation, have proven useful to separate BOLD-related components from noise components, independently from the task activities.

### 4.3. GLM analysis

Because of the high temporal resolution, the parameters for the autocorrelation correction of the residuals were expected to be higher in MREG as compared to the SMS-EPI scanning parameters. The difference in temporal resolution of SMS-EPI and MREG data was the most important factor to consider in the GLM analysis, since their spatial properties did not differ notably. To ensure correct calculation of the t-values and avoid a statistical inflation caused by the high autocorrelation of the residuals in the MREG data, properties and assumptions of the GLM were investigated.

In fMRI data analysis with conventional TRs in the order of 1–3s the autocorrelation of the residuals can be corrected using low AR model orders (1–2; (Lenoski et al., 2008), whereas for MREG we found that much higher model orders are necessary (e.g., 18) to correct for serial correlations. This is in line with recent reports on fast sampling fMRI experiments (Bollmann et al., 2018; Corbin et al., 2018). In our study, we observed an increase in the AR model orders using a TR of 100 ms. This goes in line with a recent work by (Corbin et al., 2018) where they concluded that a TR of 350 ms results in a AR model of around 12 to 15 to correct for serial correlations in the residuals. Moreover, they showed that the serial correlation is reduced when additional physiological regressors are used. This we also found in this study and observed an expected increase in the AR model orders using an even shorter TR. Different to modeling the physiological regressor (e.g., using RETRO-ICOR (Bollmann et al., 2018)) we showed that with a TR of 100 ms, it is actually possible to extract physiological components directly from the MREG signals via spatial independent component analysis, thereby avoiding the potential inaccuracies of a priori models of physiological confounds. We as well observed that a higher explained variance (e.g., by adding physiological confound predictors to the model) was linked to a lower estimated AR orders, which reflected a lower autocorrelation in the residuals. This is an important difference compared to sequences using a low TR and it is crucial to fully take advantage of the high temporal resolution of MREG sequence when modeling the expected time course in the design matrix by including specific confound predictors for cardiac pulsation and respiration related signals. Even though the inclusion of ICA component time courses as model predictors is in some cases difficult, the overall effect of improving the explained variance is expectedly the same with respect to including externally measured pulse and respiration data because of the high correlation of these time courses.

Because additional ICA component confound predictors were added to both sequences the explained variance in both sequences is highly comparable. But MREG is more sensitive to capture heartbeat and respiration information suggesting that this sequence is far more sensitive than conventional fMRI where the heartbeat information can not directly be separated from the signal because of the low temporal resolution.

While these effects are clearly visible in the single-subject analyses, the differences in the RFX group results between SMS-EPI and MREG sequences are less straightforward to explain or display. In fact, they can be caused by both the different sensitivity of the two sequences and by individual subject performance variability. All in all, more studies are necessary to clarify this matter.

In standard fMRI analysis pipelines, the detection of motion remains a problem which needs further investigation (Leonard, Flournoy, Lewis-de los Angeles and Whitaker, 2017; Todd et al., 2015; Yakupov et al., 2017). Two different correction methods, retrospective and prospective, are most often used in fMRI. Prospective motion correction shows better results in correction of motion artifacts, especially in the intra volume motion, which cannot be corrected using standard retrospective correction methods (Todd et al., 2015; Zaitsev et al., 2017). For MREG the intra

slice and volume motion correction problem is intrinsically reduced by the higher temporal resolution allowed by the acquisition method. For real-time applications prospective motion correction would be a potential solution to handle motion in real-time (Riemenschneider et al., 2019).

### 5. The impact on real-time BCI/neurofeedback experiments

Due to more and more attention to applications of real-time neuroimaging methods, specifically in the field of fMRI (Sulzer et al., 2013; Thibault et al., 2018), the implementation of a higher temporal resolution is a very important goal. We showed that physiological components are clearly visible in the MREG data and exhibited that they can be extracted to correct the measured brain signal in real-time. This allows to control for brain-modulation effects caused by changes in cardiac pulsation or respiration. This is especially important to ensure that possible improvements in behavior by using BCI/NF setups are not just caused by learning to regulate breathing but due to a real cognitive control.

### 6. Conclusion

In this manuscript we investigated the different impact of a SMS-EPI sequence and the more recently developed MREG sequence on high temporal resolution fMRI. For both sequences the same coverage and spatial resolution was used. The temporal resolution of the MREG sequence was, however, 20 times higher than the SMS-EPI sequence using a conventional TR of 2s as typically used in (real-time) fMRI recordings. Overall the results of SMS-EPI and MREG data analysis were comparable even though different preprocessing and analysis techniques needed to be adapted for the MREG compared to SMS-EPI data processing. Most importantly, a much higher AR model order of ~20 was required to correct for serial correlations in the GLM residuals. Thereby, the higher temporal resolution of MREG allows disentangling explicitly physiological influences from cardiac pulsation and respiration.

tSNR was also comparable between sequences, although known sequence-specific geometric image distortions were observed. Further research is necessary to create more detailed models for sequences using such a high temporal resolution to explain more variance which, as we showed, lowers the temporal autocorrelation in the residuals and increases the power of the statistical analysis.

This exploratory research serves a more comprehensive utilization of the findings for following rt-MREG based NF/BCI research.

### Appendix A. Supplementary data

Supplementary data to this article can be found online at https://doi.org/10.1016/j.neuroimage.2019.03.046.

# References

Akin, B., Lee, H.L., Hennig, J., LeVan, P., 2017. Enhanced subject-specific resting-state network detection and extraction with fast fMRI. Hum. Brain Mapp. 38 (2), 817–830. https://doi.org/10.1002/hbm.23420.

Assländer, J., Zahneisen, B., Hugger, T., Reisert, M., Lee, H.L., LeVan, P., Hennig, J., 2013. Single shot whole brain imaging using spherical stack of spirals trajectories. Neuroimage 73, 59–70. https://doi.org/10.1016/j.neuroimage.2013.01.065.

Barker, J.W., Aarabi, A., Huppert, T.J., 2013. Autoregressive model based algorithm for correcting motion and serially correlated errors in fNIRS. Biomed. Opt. Express 4 (8), 1366. https://doi.org/10.1364/BOE.4.001366.

Barker, J.W., Rosso, A.L., Sparto, P.J., Huppert, T.J., 2016. Correction of motion artifacts and serial correlations for real-time functional near-infrared spectroscopy. Neurophotonics 3 (3), 031410. https://doi.org/10.1117/1.NPh.3.3.031410.

Barth, M., Breuer, F., Koopmans, P.J., Norris, D.G., Poser, B.A., 2016. Simultaneous multislice (SMS) imaging techniques. Magn. Reson. Med. 75 (1), 63–81. https://doi.org/10.1002/mrm.25897.

Bastos, A.M., Schoffelen, J.-M., 2016. A tutorial review of functional connectivity analysis methods and their interpretational pitfalls. Front. Syst. Neurosci. 9, 175. https://doi.org/10.3389/fnsys.2015.00175.

Bollmann, S., Puckett, A.M., Cunnington, R., Barth, M., 2018. Serial correlations in single-subject fMRI with sub-second TR. Neuroimage 166, 152–166. https://doi.org/10.1016/j.neuroimage.2017.10.043.

Boynton, G.M., Engel, S.A., Glover, G.H., Heeger, D.J., 1996. Linear systems analysis of functional magnetic resonance imaging in human V1. J. Neurosci. 16 (13), 4207–4221. https://doi.org/10.1523/JNEUROSCI.16-13-04207.1996.

Burg, J.P., 1975. Maximum entropy spectral analysis. Astron. Astrophys. Suppl. 15, 383. Retrieved from. http://labs.adsabs.harvard.edu/adsabs/abs/1974A&AS...15..383A/.

Canuet, L., 2015. Neurorehabilitation in stroke: the Role of functional connectivity. Int. J. Neurorehabil. 02 (03), 1–2. https://doi.org/10.4172/2376-0281.1000172.

Chen, J.E., Polimeni, J.R., Bollmann, S., Glover, G.H., 2019. On the analysis of rapidly sampled fMRI data. Neuroimage 188, 807–820. https://doi.org/10.1016/J.NEUROIMAGE.2019.02.008.

Chen, L., T Vu, A., Xu, J., Moeller, S., Ugurbil, K., Yacoub, E., Feinberg, D.A., 2015. Evaluation of highly accelerated simultaneous multi-slice EPI for fMRI. Neuroimage 104, 452–459. https://doi.org/10.1016/j.neuroimage.2014.10.027.

Corbin, N., Todd, N., Friston, K.J., Callaghan, M.F., 2018. Accurate modeling of temporal correlations in rapidly sampled fMRI time series. Hum. Brain Mapp. 39 (10), 3884–3897. https://doi.org/10.1002/hbm.24218.

De Hoon, M.J.L., Van Der Hagen, T.H.J.J., Schoonewelle, H., Van Dam, H., 1996. Why Yule-Walker should not be used for autoregressive modelling. Ann. Nucl. Energy 23 (15), 1219–1228. https://doi.org/10.1016/0306-4549(95)00126-3.

De Martino, F., Gentile, F., Esposito, F., Balsi, M., Di Salle, F., Goebel, R., Formisano, E., 2007. Classification of fMRI independent components using IC-fingerprints and support vector machine classifiers. Neuroimage 34 (1), 177–194. https://doi.org/10.1016/j.neuroimage.2006.08.041.

Díez-Cirarda, M., Ojeda, N., Peña, J., Cabrera-Zubizarreta, A., Lucas-Jiménez, O., Gómez-Esteban, J.C., et al., 2017. Increased brain connectivity and activation after cognitive rehabilitation in Parkinson's disease: a randomized controlled trial. Brain Imag. Behav. 11 (6), 1640–1651. https://doi.org/10.1007/s11682-016-9639-x.

Eklund, A., Friman, O., Andersson, M., Knutsson, H., 2011. Comparing fMRI Activity Maps from GLM and CCA at the Same Significance Level by Fast Random Permutation Tests on the GPU. Retrieved from. http://www.diva-portal.org/smash/record.jsf?pid=diva2:402372.

Fadili, M.J., Ruan, S., Bloyet, D., Mazoyer, B., 2003. Analysis of fMRI time series. Human Brain Function 178 (1), 160–178. https://doi.org/10.1006/nimg.1995.1007.

Feinberg, D.A., Moeller, S., Smith, S.M., Auerbach, E., Ramanna, S., Glasser, M.F., et al., 2010. Multiplexed echo planar imaging for sub-second whole brain fmri and fast diffusion imaging. PLoS One 5 (12), e15710. https://doi.org/10.1371/journal.pone.0015710.

Feinberg, D.A., Setsompop, K., 2013. Ultra-fast MRI of the human brain with simultaneous multi-slice imaging. J. Magn. Reson. 229, 90–100. https://doi.org/10.1016/j.jmr.2013.02.002.

Feinberg, D.A., Yacoub, E., 2012. The rapid development of high speed, resolution and precision in fMRI. Neuroimage 62 (2), 720–725. https://doi.org/10.1016/j.neuroimage.2012.01.049.

Friman, O., Westin, C.F., 2005. Resampling fMRI time series. Neuroimage 25 (3), 859–867. https://doi.org/10.1016/j.neuroimage.2004.11.046.

Friston, K.J., 2011. Functional and effective connectivity: a review. Brain Connect. 1 (1), 13–36. https://doi.org/10.1089/brain.2011.0008.

Friston, K.J., Josephs, O., Zarahn, E., Holmes, A.P., Rouquette, S., Poline, J.B., 2000. To smooth or not to smooth? Bias and efficiency in fMRI time-series analysis. Neuroimage 12 (2), 196–208. https://doi.org/10.1006/nimg.2000.0609.

Glover, G.H., 1999. Deconvolution of impulse response in event-related BOLD fMRI. Neuroimage 9 (4), 416–429. https://doi.org/10.1006/nimg.1998.0419.

Greve, D.N., Fischl, B., 2009. Accurate and robust brain image alignment using boundary-based registration. Neuroimage 48 (1), 63–72. https://doi.org/10.1016/j.neuroimage.2009.06.060.

Gulban, O.F., Schneider, M., 2016. Segmentator: v1.1.0. https://doi.org/10.5281/ZENODO.157996.

Hao, Y., Khoo, H.M., von Ellenrieder, N., Gotman, J., 2017. Subject-level reliability analysis of fast fMRI with application to epilepsy. Magn. Reson. Med. 78 (1), 370–382. https://doi.org/10.1002/mrm.26365.

Hennig, J., Zhong, K., Speck, O., 2007. MR-Encephalography: fast multi-channel monitoring of brain physiology with magnetic resonance. Neuroimage 34 (1), 212–219. https://doi.org/10.1016/j.neuroimage.2006.08.036.

Holmes, C.J., Hoge, R., Collins, L., Woods, R., Toga, A.W., Evans, A.C., 1998. Enhancement of MR images using registration for signal averaging. J. Comput. Assist. Tomogr. 22 (2), 324–333. https://doi.org/10.1097/00004728-199803000-00032.

Hsu, Y.C., Chu, Y.H., Tsai, S.Y., Kuo, W.J., Chang, C.Y., Lin, F.H., 2017. Simultaneous multi-slice inverse imaging of the human brain. Sci. Rep. 7 (1), 17019. https://doi.org/10.1038/s41598-017-16976-0.

Hu, X., Yacoub, E., 2012. The story of the initial dip in fMRI. Neuroimage 62 (2), 1103–1108. https://doi.org/10.1016/j.neuroimage.2012.03.005.

Hutchison, R.M., Womelsdorf, T., Allen, E.A., Bandettini, P.A., Calhoun, V.D., Corbetta, M., et al., 2013. Dynamic functional connectivity: promise, issues, and interpretations. Neuroimage 80, 360–378. https://doi.org/10.1016/j.neuroimage.2013.05.079.

Hyvärinen, A., 1999. Fast and robust fixed-point algorithms for independent component analysis. IEEE Trans. Neural Netw. 10 (3), 626–634. https://doi.org/10.1109/72.761722.

Kairov, U., Cantini, L., Greco, A., Molkenov, A., Czerwinska, U., Barillot, E., Zinovyev, A., 2017. Determining the optimal number of independent components for reproducible transcriptomic data analysis. BMC Genomics 18 (1), 712. https://doi.org/10.1186/s12864-017-4112-9.

Kanwisher, N.G., McDermott, J., Chun, M.M., 1997. The fusiform face area: a module in human extrastriate cortex specialized for face perception. J. Neurosci. 17 (11), 4302–4311. https://doi.org/10.1523/JNEUROSCI.17-11-04302.1997.

Karahanoğlu, F.I., Van De Ville, D., 2017. Dynamics of large-scale fMRI networks: deconstruct brain activity to build better models of brain function. Curr. Opin. Biomed. Eng. 3, 28–36. https://doi.org/10.1016/j.cobme.2017.09.008.

Kay, S.M., Marple, S.L., 1981. Spectrum analysis—a modern perspective. Proc. IEEE 69 (11), 1380–1419. In: https://doi.org/10.1109/PROC.1981.12184.

Klein, A., Andersson, J., Ardekani, B.A., Ashburner, J., Avants, B., Chiang, M.-C., et al., 2009. Evaluation of 14 nonlinear deformation algorithms applied to human brain MRI registration. Neuroimage 46 (3), 786–802. https://doi.org/10.1016/j.neuroimage.2008.12.037.

Kornbrot, D., 2014. Spearman's Rho. Wiley StatsRef: Statistics Reference Online. John Wiley & Sons, Ltd, Chichester, UK. https://doi.org/10.1002/9781118445112.stat06541.

Krause, F., Benjamins, C., Lührs, M., Eck, J., Noirhomme, Q., Rosenke, M., et al., 2017. Real-time fMRI-based self-regulation of brain activation across different visual feedback presentations. Brain-Computer Interfaces 4 (1–2), 87–101. https://doi.org/10.1080/2326263X.2017.1307096.

Lee, H.L., Zahneisen, B., Hugger, T., LeVan, P., Hennig, J., 2013. Tracking dynamic resting-state networks at higher frequencies using MR-encephalography. Neuroimage 65, 216–222. https://doi.org/10.1016/j.neuroimage.2012.10.015.

Lenoski, B., Baxter, L.C., Karam, L.J., Maisog, J., Debbins, J., 2008. On the performance of autocorrelation estimation algorithms for fMRI analysis. IEEE J. Selected Top. Signal Proces. 2 (6), 828–838. https://doi.org/10.1109/JSTSP.2008.2007819.

Leonard, J., Flournoy, J., Lewis-de los Angeles, C.P., Whitaker, K., 2017. How much motion is too much motion? Determining motion thresholds by sample size for reproducibility in developmental resting-state MRI. Research Ideas and Outcomes 3, e12569. https://doi.org/10.3897/rio.3.e12569.

Lewis, L.D., Setsompop, K., Rosen, B.R., Polimeni, J.R., 2016. Fast fMRI can detect oscillatory neural activity in humans. Proc. Natl. Acad. Sci. Unit. States Am. 113 (43), E6679–E6685. https://doi.org/10.1073/pnas.1608117113.

LI, S.-M., 2014. Burmanesque mini review. Adv. Synth. Catal. 1–6. https://doi.org/10.1002/adsc.201, 201.

Lin, F.H., Tsai, K.W.K., Chu, Y.H., Witzel, T., Nummenmaa, A., Raij, T., et al., 2012. Ultrafast inverse imaging techniques for fMRI. Neuroimage 62 (2), 699–705. https://doi.org/10.1016/j.neuroimage.2012.01.072.

Locascio, J.J., Jennings, P.J., Moore, C.I., Corkin, S., 1997. Time series analysis in the time domain and resampling methods for studies of functional magnetic resonance brain imaging. Hum. Brain Mapp. 5 (3), 168–193. https://doi.org/10.1002/(SICI)1097-0193(1997)5:3<168. AID-HBM3>3.0.CO;2-1.

Lührs, M., Sorger, B., Goebel, R., Esposito, F., 2017. Automated selection of brain regions for real-time fMRI brain-computer interfaces. J. Neural Eng. 14 (1), 016004. https://doi.org/10.1088/1741-2560/14/1/016004.

McKeown, M.J., 2000. Detection of consistently task-related activations in fMRI data with hybrid independent component analysis. Neuroimage 11 (1), 24–35. https://doi.org/10.1006/nimg.1999.0518.

McKeown, M.J., Hansen, L.K., Sejnowsk, T.J., 2003. Independent component analysis of functional MRI: what is signal and what is noise? Curr. Opin. Neurobiol. 13 (5), 620–629. https://doi.org/10.1016/j.conb.2003.09.012.

McKeown, M.J., Makeig, S., Brown, G.G., Jung, T.P., Kindermann, S.S., Bell, A.J., Sejnowski, T.J., 1998. Analysis of fMRI data by blind separation into independent spatial components. Hum. Brain Mapp. 6 (3), 160–188. https://doi.org/10.1002/(SICI)1097-0193(1998)6:3<160. AID-HBM5>3.0.CO;2-1.

Moeller, S., Yacoub, E., Olman, C.A., Auerbach, E., Strupp, J., Harel, N., Uğurbil, K., 2010. Multiband multislice GE-EPI at 7 tesla, with 16-fold acceleration using partial parallel imaging with application to high spatial and temporal whole-brain FMRI. Magn. Reson. Med. 63 (5), 1144–1153. https://doi.org/10.1002/mrm.22361.

Monti, M.M., 2011. Statistical analysis of fMRI time-series: a critical review of the GLM approach. Front. Hum. Neurosci. 5, 28. https://doi.org/10.3389/fnhum.2011.00028.

Murphy, K., Bodurka, J., Bandettini, P.A., 2007. How long to scan? The relationship between fMRI temporal signal to noise ratio and necessary scan duration. Neuroimage 34 (2), 565–574. https://doi.org/10.1016/j.neuroimage.2006.09.032.

Nicholson, A.A., Rabellino, D., Densmore, M., Frewen, P.A., Paret, C., Kluetsch, R., et al., 2017. The neurobiology of emotion regulation in posttraumatic stress disorder: amygdala downregulation via real-time fMRI neurofeedback. Hum. Brain Mapp. 38 (1), 541–560. https://doi.org/10.1002/hbm.23402.

Ochmann, S., Dyrba, M., Grothe, M.J., Kasper, E., Webel, S., Hauenstein, K., Teipel, S.J., 2017. Does functional connectivity provide a marker for cognitive rehabilitation effects in alzheimer's disease? An interventional study. J. Alzheimer's Dis. 57 (4), 1303–1313. https://doi.org/10.3233/JAD-160773.

Peterson, B.S., Skudlarski, P., Gatenby, J.C., Zhang, H., Anderson, A.W., Gore, J.C., 1999. An fMRI study of stroop word-color interference: evidence for cingulate subregions subserving multiple distributed attentional systems. Biol. Psychiatry 45 (10), 1237–1258. https://doi.org/10.1016/S0006-3223(99)00056-6.

Pfeuffer, J., Van Moortele, P. F. De, Ugurbil, K., Hu, X., Glover, G.H., 2002. Correction of physiologically induced global off-resonance effects in dynamic echo-planar and spiral functional imaging. Magn. Reson. Med. 47 (2), 344–353. https://doi.org/10.1002/mrm.10065.

Pollock, D.S.G., Green, R.C., 1999. Handbook of Time Series Analysis, Signal Processing, and Dynamics. Handbook of Time Series Analysis, Signal Processing, and Dynamics. https://doi.org/10.1016/B978-012560990-6/50000-2.

Poser, B.A., Setsompop, K., 2018. Pulse sequences and parallel imaging for high spatiotemporal resolution MRI at ultra-high field. Neuroimage 168, 101–118. https://doi.org/10.1016/J.NEUROIMAGE.2017.04.006.

Posse, S., Ackley, E., Mutihac, R., Rick, J., Shane, M., Murray-Krezan, C., et al., 2012. Enhancement of temporal resolution and BOLD sensitivity in real-time fMRI using multi-slab echo-volumar imaging. Neuroimage 61 (1), 115–130. https://doi.org/10.1016/j.neuroimage.2012.02.059.

Posse, S., Ackley, E., Mutihac, R., Zhang, T., Hummatov, R., Akhtari, M., et al., 2013. High-Speed real-time resting-state fMRI using multi-slab echo-volumar imaging. Front. Hum. Neurosci. 7, 479. https://doi.org/10.3389/fnhum.2013.00479.

Rabrait, C., Ciuciu, P., Ribés, A., Poupon, C., Le Roux, P., Dehaine-Lambertz, G., et al., 2008. High temporal resolution functional MRI using parallel echo volumar imaging. J. Magn. Reson. Imaging 27 (4), 744–753. https://doi.org/10.1002/jmri.21329.

Riemenschneider, B., LeVan, P., Hennig, J., 2019. Targeted partial reconstruction for real-time fMRI with arbitrary trajectories. Magn. Reson. Med. 81 (2), 1118–1129. https://doi.org/10.1002/mrm.27478.

Riemenschneider, B., Levan, P., Reisert, M., Hennig, J., 2015. Nonlinear trajectories in real-time fMRI using target volumes. Abstract #2055 4 (7), 232908. Retrieved from. https://dev.ismrm.org/2015/2055.html.

Rogers, B.P., Katwal, S.B., Morgan, V.L., Asplund, C.L., Gore, J.C., 2010. Functional MRI and multivariate autoregressive models. Magn. Reson. Imag. 28 (8), 1058–1065. https://doi.org/10.1016/j.mri.2010.03.002.

Sahib, A.K., Erb, M., Marquetand, J., Martin, P., Elshahabi, A., Klamer, S., Focke, N.K., 2018. Evaluating the impact of fast-fMRI on dynamic functional connectivity in an event-based paradigm. PLoS One 13 (1) e0190480. https://doi.org/10.1371/journal.pone.0190480.

Setsompop, K., Gagoski, B.A., Polimeni, J.R., Witzel, T., Wedeen, V.J., Wald, L.L., 2012. Blipped-controlled aliasing in parallel imaging for simultaneous multislice echo planar imaging with reduced g-factor penalty. Magn. Reson. Med. 67 (5), 1210–1224. https://doi.org/10.1002/mrm.23097.

Sorger, B., Reithler, J., Dahmen, B., Goebel, R., 2012. A real-time fMRI-based spelling device immediately enabling robust motor-independent communication. Curr. Biol. 22 (14), 1333–1338. https://doi.org/10.1016/j.cub.2012.05.022.

Sulzer, J., Haller, S., Scharnowski, F., Weiskopf, N., Birbaumer, N., Blefari, M.L., et al., 2013. Real-time fMRI neurofeedback: progress and challenges. Neuroimage 76, 386–399. https://doi.org/10.1016/j.neuroimage.2013.03.033.

Tak, S., Ye, J.C., 2014. Statistical analysis of fNIRS data: a comprehensive review. Neuroimage 85, 72–91. https://doi.org/10.1016/j.neuroimage.2013.06.016.

Thibault, R.T., MacPherson, A., Lifshitz, M., Roth, R.R., Raz, A., 2018. Neurofeedback with fMRI: A Critical Systematic Review, 172 NeuroImage §. Academic Press. https://doi.org/10.1016/j.neuroimage.2017.12.071.

Todd, N., Josephs, O., Callaghan, M.F., Lutti, A., Weiskopf, N., 2015. Prospective motion correction of 3D echo-planar imaging data for functional MRI using optical tracking. Neuroimage 113, 1–12. https://doi.org/10.1016/j.neuroimage.2015.03.013.

Uga, M., Dan, I., Sano, T., Dan, H., Watanabe, E., 2014. Optimizing the general linear model for functional near-infrared spectroscopy: an adaptive hemodynamic response function approach. Neurophotonics 1 (1), 015004. https://doi.org/10.1117/1.NPh.1.1.015004.

Welvaert, M., Rosseel, Y., 2013. On the definition of signal-to-noise ratio and contrast-to-noise ratio for fMRI data. PLoS One 8 (11), e77089. https://doi.org/10.1371/journal.pone.0077089.

Yakupov, R., Lei, J., Hoffmann, M.B., Speck, O., 2017. False fMRI activation after motion correction. Hum. Brain Mapp. 38 (9), 4497–4510. https://doi.org/10.1002/hbm.23677.

Zahneisen, B., Grotz, T., Lee, K.J., Ohlendorf, S., Reisert, M., Zaitsev, M., Hennig, J., 2011. Three-dimensional MR-encephalography: fast volumetric brain imaging using rosette trajectories. Magn. Reson. Med. 65 (5), 1260–1268. https://doi.org/10.1002/mrm.22711.

Zahneisen, B., Hugger, T., Lee, K.J., Levan, P., Reisert, M., Lee, H.L., et al., 2012. Single shot concentric shells trajectories for ultra fast fMRI. Magn. Reson. Med. 68 (2), 484–494. https://doi.org/10.1002/mrm.23256.

Zaitsev, M., Akin, B., LeVan, P., Knowles, B.R., 2017. Prospective motion correction in functional MRI. Neuroimage 154, 33–42. https://doi.org/10.1016/j.neuroimage.2016.11.014.

Zilverstand, A., Sorger, B., Zimmermann, J., Kaas, A., Goebel, R., 2014. Windowed correlation: a suitable tool for providing dynamic fMRI-based functional connectivity neurofeedback on task difficulty. PLoS One 9 (1), e85929. https://doi.org/10.1371/journal.pone.0085929.